Seeking Anderson's faulting in seismicity: A centennial celebration

Bernard Celerier

SEEKING ANDERSON'S FAULTING IN SEISMICITY: A CENTENNIAL CELEBRATION

Bernard Célérier[1]

Received 14 August 2007; accepted 3 April 2008; published 1 October 2008.

[1] The reactivation of faults with near-optimal orientations is commonly considered to control the state of stress in the crust. Near the surface, where a principal stress direction is vertical, the attitude of such faults is explained by Anderson's theory. This raises the questions of how prevalent this type of faulting actually is in current seismicity, down to what depth it frequently occurs, and what range of friction angles explains it best. The Global Centroid Moment Tensor catalog is analyzed to address these questions. Dip-slip and strike-slip mechanisms are dominant, and oblique slips are relatively rare for well-constrained events with depths shallower than 30 km. Preferred Andersonian faulting is the simplest, but not the unique, explanation for this dominance. Isolating reverse, strike-slip, and normal events reveals an asymmetry in the distribution of nodal plane dips and plunges of the *P*, *B*, and *T* axes between reverse and normal faulting. Assuming that the most frequent events correspond to reactivation near optimal orientations yields 40–60° and 0–20° friction angles for reverse and normal faults, respectively. This indicates that reverse and normal faulting mechanics are not symmetrical with respect to stress configuration as predicted by Anderson's theory.

Citation: Célérier, B. (2008), Seeking Anderson's faulting in seismicity: A centennial celebration, *Rev. Geophys.*, *46*, RG4001, doi:10.1029/2007RG000240.

1. INTRODUCTION

[2] Ernest M. Anderson proposed the simplest, yet realistic, theory that relates faulting to the state of stress to the Edinburgh Geological Society about a century ago [*Anderson*, 1905]. Walter Bucher derived strikingly similar concepts a few years later [*Bucher*, 1920, 1921].

[3] This theory of faulting is based on the three simple assumptions (1) that rocks can be considered isotropic as a first approximation, (2) that they fail along shear planes when the state of stress satisfies a *Coulomb* [1776] failure criterion, and (3) that the Earth's free surface requires a principal stress direction to be vertical. The reliance on "the simplest and most important" [*Jaeger and Cook*, 1979] failure criterion and the ability to relate the three major types of faulting, normal, strike slip, and reverse, to three possible attitudes of the principal stress directions gave this theory a deep influence that persists to this day.

[4] However, it has also been clear since its outset that this theory cannot explain all types of faulting because of two main limitations. First, it predicts slip to be along the fault plane strike or dip direction only and therefore does not account for frequently observed oblique slips. Second, if assuming isotropy simplifies the theory by locating failure on two optimally oriented conjugate fault planes only, it is not consistent with the fact that most often slip occurs on preexisting faults, therefore within an anisotropic material containing planes of weakness.

[5] The model of frictional slip on a preexisting plane of weakness overcame the isotropy assumption [*Wallace*, 1951; *Bott*, 1959; *Jaeger*, 1960; *McKenzie*, 1969], and rotation of the principal stress axes away from the vertical direction at depth was proposed as an explanation for oblique slips [*Anderson*, 1905; *Hafner*, 1951; *Williams*, 1958]. A widely relevant alternate explanation for oblique slips that does not require rotated stress axes was also found in the model of frictional slip on a nonoptimally oriented plane of weakness [*Wallace*, 1951; *Bott*, 1959].

[6] The compilation of homogeneous worldwide earthquake source parameter databases such as the Global Centroid Moment Tensor catalog [*Dziewonski et al.*, 1981; *Dziewonski and Woodhouse*, 1983; *Jost and Herrmann*, 1989; *Frohlich and Apperson*, 1992; *Jackson*, 2002; *Ekström et al.*, 2005] and the development of methods to assess the reliability of these data [*Frohlich and Davis*, 1999] provide an opportunity to analyze the relative importance of three scenarios: (1) Anderson's faulting, (2) frictional slip on a preexisting fault, and (3) rotated principal stress axes. An analysis of the geometry of focal mechanisms of shallow focus (depth within 0–30 km) earthquakes suggests prevalent Andersonian conditions on one hand [*Frohlich*, 2001], yet reveals an asymmetry between normal and reverse faulting that contradicts Anderson's theory on the other

[1]Geosciences Montpellier, Université de Montpellier II, CNRS, Montpellier, France.

8755-1209/08/2007RG000240
Paper number 2007RG000240

hand, as will be shown here. Which of these three scenarios prevails in crustal deformation is a subject of interest for multiple reasons including the use of faulting as a stress indicator, the frictional paradox of slip on low-dip-angle normal faults, and the strength of the brittle crust.

[7] Simple geometrical methods have been proposed to derive the principal stress orientations from fault plane and slip orientations [*Bucher*, 1920, 1921; *Compton*, 1966; *Etchecopar*, 1984] and from earthquake focal mechanisms, albeit with an additional uncertainty when the fault plane is not distinguished from the two nodal planes [*Raleigh et al.*, 1972; *Molnar and Chen*, 1982]. Although these methods are justified in the case of Anderson faulting, using them in the more common case of slip on a preexisting fault can lead to angular errors reaching 90° [*McKenzie*, 1969; *Célérier*, 1988]. How much principal stress directions can deviate from the vertical at depth to overcome the frictional paradox of slip on low-dip-angle normal faults is the subject of ongoing debate [*Yin*, 1989; *Bradshaw and Zoback*, 1988; *Melosh*, 1990; *Wills and Buck*, 1997; *Westaway*, 1999].

[8] There is a current consensus that the magnitude of differential stress in the brittle crust is controlled by slip on faults with coefficients of friction around 0.6 [*Byerlee*, 1978] and with a sufficiently wide range of orientations to include those nearly optimal with respect to any state of stress [*Brace and Kohlstedt*, 1980; *Kohlstedt et al.*, 1995]. This scenario is supported by borehole stress magnitude measurements [*Zoback and Healy*, 1984; *Zoback et al.*, 1993; *Townend and Zoback*, 2000]. However, within the scale of this framework, the brittle crust is considered uniformly weak in any direction and thus mechanically isotropic [*Talobre*, 1957; *Jaeger*, 1962]. The characteristics of the active faults that control the state of stress near the surface, where a principal stress direction is vertical, should then be compatible with Anderson's theory because all its assumptions are satisfied. Considerations of the layered rheology of the lithosphere or of the distribution of deformation also raise the same question of whether slip partitioning along dip and strike is favored in upper crustal faulting [*McKenzie and Jackson*, 1983; *Richard and Cobbold*, 1990; *Molnar*, 1992].

[9] The work presented in this paper proposes to review this question by focusing on the characterization of Anderson's faulting in global earthquake fault plane solutions and was initiated to celebrate the centenary of Anderson's contribution [*Célérier*, 2005]. In a first step, both Anderson's theory and frictional reactivation will be reviewed. It will be argued that frictional reactivation on planes with orientation close to optimal results in a faulting geometry similar to that of Anderson's theory that will be qualified as "near Andersonian." It will then be shown that this "near-Andersonian" faulting prevails under "standard" fault and stress conditions that will be defined and that therefore, determining its prevalence is a way of evaluating the relative importance of these "standard" conditions with respect to other conditions that include low friction coefficient, high pore pressure, or rotated stress axes. In a second step, we will address how Anderson's faulting can be identified in seismological source parameters such as dip of nodal planes, slip rake, and orientations of the *P*, *B*, and *T* axes. In a third step, the data of the Global Centroid Moment Tensor catalog will be reduced to those with well-constrained orientations. They will then be sorted by depth in order to assess the relative importance of Andersonian faulting as the distance to the stress-free surface decreases. Finally, the best candidates for Andersonian faulting within shallow depth (0–30 km) will be extracted to characterize their geometry and its mechanical implications.

2. FAULTING AND SLIDING

[10] In this section, Andersonian faulting and frictional reactivation are reviewed to argue that as the range of orientations spanned by preexisting fractures in a rock mass widens, the predictions of these two models become more and more similar. This is because frictional slip requires less stress difference as the plane orientation becomes closer to that of the optimal conjugate planes. Thus, as more and more weak plane orientations become available, those activated become closer and closer to optimal. Within shallow crust this leads to a situation similar to that of Andersonian faulting. These two cases will then be grouped and called "near-Andersonian" faulting.

[11] In the case where the number of available weak orientations is small, those activated may differ significantly from the optimal ones. However, a statistical bias toward optimal orientations is expected when grouping a large number of such cases.

2.1. Andersonian Faulting

[12] The first premise of Anderson's theory is that rupture is controlled by a *Coulomb* [1776] criterion (variables are defined in Table 1):

$$\tau = \tau_0 + \mu\sigma_n, \tag{1}$$

where τ is the shear stress, σ_n is the normal stress, τ_0 is the cohesion, and μ is the coefficient of internal friction, related to the angle of internal friction, φ_0, by

$$\mu = \tan(\varphi_0). \tag{2}$$

The second premise is that the medium is isotropic, so that rupture occurs when the applied stress on the most favorably oriented planes reaches the Coulomb rupture criterion (Figure 1a). This requires a stress difference threshold to be reached. Subtracting pore pressure from total stress to obtain the effective principal stress magnitudes, $\sigma_1 \geq \sigma_2 \geq \sigma_3$ (compression being positive), and defining the normalized stress difference, s_0, as

$$s_0 = \frac{(\sigma_1 - \sigma_3)}{\sigma_1}, \tag{3}$$

this requirement can be expressed as

$$s_0 \geq s_t(\mu, \tau_0, \sigma_1), \tag{4}$$

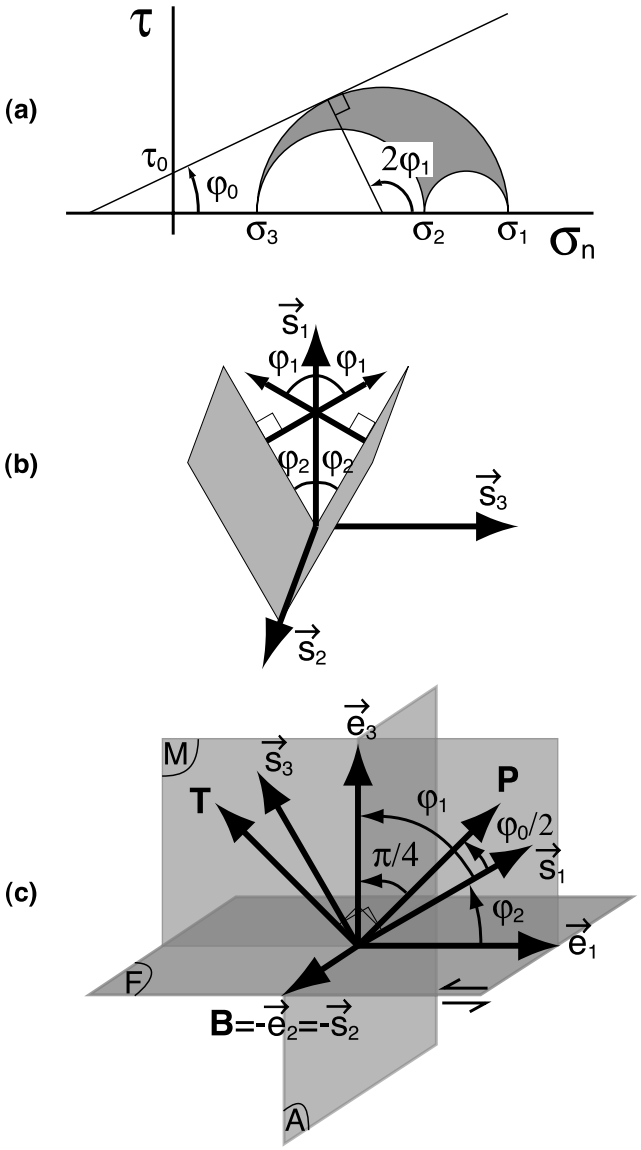

Figure 1. Optimal plane orientation and applied stress. (a) *Mohr*'s [1882] plane. (b) Orientation of the optimal conjugate planes with respect to the principal stress directions. (c) Principal stress and *P*, *B*, and *T* axis orientations with respect to an active optimal plane with known slip direction. F, fault plane; A, auxiliary nodal plane; M, plane of movement [*Arthaud*, 1969]. Other symbols are defined in Table 1.

with

$$s_t(\mu, \tau_0, \sigma_1) = \left(1 + \frac{\tau_0}{\mu\sigma_1}\right) s_c(\mu), \tag{5}$$

where $s_c(\mu)$ depends only on the coefficient of friction

$$s_c(\mu) = 2\mu\left(\sqrt{1+\mu^2} - \mu\right) \tag{6}$$

or, alternatively, on the friction angle

$$s_c(\varphi_0) = \frac{2\sin\varphi_0}{1+\sin\varphi_0} = \frac{2\tan\varphi_0}{\tan\varphi_1} = \frac{\sin\varphi_0}{\sin^2\varphi_1}, \tag{7}$$

with

$$\varphi_1 = \frac{\varphi_0}{2} + \frac{\pi}{4}. \tag{8}$$

[13] When cohesion is negligible with respect to stress magnitudes, equation (5) can be reduced to

$$s_t(\mu, \tau_0, \sigma_1) \approx s_c(\mu). \tag{9}$$

This formulation (equation (4)) encapsulates two different stress paths leading s_0 to the rupture threshold: one where the stress difference numerator increases at constant denominator and the other where the maximum effective stress denominator decreases as pore pressure increases at constant numerator. The range of the s_t (μ, τ_0, σ_1) threshold for crustal rocks can be estimated from values of s_0 reached at failure during triaxial tests from *Brace* [1964], *Brace et al.* [1966], *Byerlee* [1967], *Mogi* [1965, 1966a, 1996b], and *Matsushima* [1959, 1960] and also compiled by *Ohnaka* [1973] and *Sheorey* [1997]. The decreasing trend of this threshold with respect to σ_1 (Figure 2) results from the superposition of three factors: the inverse dependence on σ_1 (equation (5)) and also the increase of the apparent cohesion, τ_0, and the decrease of the apparent angle of internal friction, φ_0, that are defined by the tangential approximation of the rupture envelope which is typically concave downward (see compilation by *Lockner* [1995]).

[14] The plane of rupture can be located within the direct orthogonal frame of principal stress unit eigenvectors, $\mathbf{s}_1$, $\mathbf{s}_2$, and $\mathbf{s}_3$, corresponding to the eigenvalues σ_1, σ_2, and σ_3: it occurs along either of the two conjugate planes that contain $\mathbf{s}_2$ and have a normal at angle φ_1 from $\mathbf{s}_1$ (Figure 1b). If the slip direction is further assumed to be along the shear stress direction, it is then normal to $\mathbf{s}_2$ within each plane.

[15] Conversely, the orientations of the principal stresses can be determined from the fault plane and slip orientation (Figure 1c). Defining the fault and slip orthogonal frame of unit vectors, $\mathbf{e}_1$, $\mathbf{e}_2$, and $\mathbf{e}_3$, as in the work by *McKenzie* [1969], where $\mathbf{e}_3$ is normal to the plane and points to what is defined as the upper half-space, $\mathbf{e}_1$ is along the slip of the lower half-space with respect to the upper half-space, and $\mathbf{e}_2$ is normal to both $\mathbf{e}_1$ and $\mathbf{e}_3$ and chosen so that the frame is direct, then $\mathbf{s}_1$, $\mathbf{s}_2$, and $\mathbf{s}_3$ are obtained by rotating $\mathbf{e}_1$, $\mathbf{e}_2$, and $\mathbf{e}_3$ by an angle φ_2 around $-\mathbf{e}_2$, with

$$\varphi_2 = \frac{\pi}{4} - \frac{\varphi_0}{2} = \frac{\pi}{2} - \varphi_1. \tag{10}$$

Three perpendicular planes are thus convenient to consider: the fault plane that contains $\mathbf{e}_1$, $\mathbf{e}_2$, and $\mathbf{s}_2$, the auxiliary plane of a fault plane solution that contains $\mathbf{e}_2$, $\mathbf{e}_3$, and $\mathbf{s}_2$, and the plane of movement that contains $\mathbf{e}_1$, $\mathbf{e}_3$, $\mathbf{s}_1$, and $\mathbf{s}_3$ [*Arthaud*, 1969]. This has been used to infer the stress orientation from a single fault and slip datum or from a pair of conjugate faults [*Bucher*, 1920, 1921; *Compton*, 1966; *Etchecopar*, 1984]. In the case of conjugate faults, this method requires the slip on each plane to be perpendicular to the intersection of the fault planes and yields inconsistent

TABLE 1. Meanings of Symbols

Symbol	Equations	Comments
	Stress	
$\mathbf{T_e}$		effective stress tensor
$\mathbf{s}_1$, $\mathbf{s}_2$, and $\mathbf{s}_3$		principal stress directions frame (eigenvectors of $\mathbf{T_e}$)
$\sigma_1 \geq \sigma_2 \geq \sigma_3$	(3), (5), (11), and (15)	principal effective stress magnitudes (eigenvalues of $\mathbf{T_e}$)
$r_0 = \frac{\sigma_1-\sigma_2}{\sigma_1-\sigma_3}$	(11)	stress tensor aspect ratio
$s_0 = \frac{(\sigma_1-\sigma_3)}{\sigma_1}$	(3) and (4)	normalized stress difference
τ	(1), (12), and (13)	shear stress
σ_n	(1), (12), and (13)	effective normal stress
	Failure or Friction	
τ_0	(1) and (5)	cohesion
$\mu = \tan(\varphi_0)$	(1), (2), (5), and (6)	coefficient of friction (standard value: 0.6)
φ_0	(2), (7), (8), (10), (16), (17), and (18)	angle of friction (standard value: 31°)
$\varphi_1 = \frac{\varphi_0}{2} + \frac{\pi}{4}$	(7), (8), (10), and (18)	(standard value: 30°)
$\varphi_2 = \frac{\pi}{4} - \frac{\varphi_0}{2}$	(10) and (17)	(standard value: 60°)
$s_c = \frac{2\tan\varphi_0}{\tan\varphi_1}$	(5), (6), (7), (9), and (14)	failure threshold for s_0 when cohesion is naught (standard value: 0.68)
$s_t = \left(1 + \frac{\tau_0}{\mu\sigma_1}\right)s_c$	(4), (5), (9), (14), and (15)	failure threshold for s_0 with cohesion
	Fault Plane	
$\mathbf{e}_3$		fault plane normal pointing toward upper half space
$\mathbf{e}_1$		slip direction of lower with respect to upper half space
$\mathbf{e}_2$		normal to $\mathbf{e}_1$ and $\mathbf{e}_3$ chosen so that $\mathbf{e}_1$, $\mathbf{e}_2$, and $\mathbf{e}_3$ are direct
	Seismic Moment Tensor	
$\mathbf{M}$	(22) and (24)	seismic moment tensor (isotropic component set to zero)
P, B, and T		eigenvectors of $\mathbf{M}$
m_P, m_B, and m_T	(25)	eigenvalues of $\mathbf{M}$
m_{ij}	(22)	components of $\mathbf{M}$
$\mathbf{DM}$	(23) and (24)	seismic moment tensor error
dm_{ij}	(23)	components of $\mathbf{DM}$
E_{rel}	(20) and (24)	relative error on the determination of $\mathbf{M}$
M_w		moment magnitude
n_{free}	(19)	number of components of $\mathbf{M}$ inverted for
f_{clvd}	(21) and (25)	compensated linear vector dipole component

results otherwise. In the case of focal mechanisms where the fault plane is not determined, this justifies approximating the P, B, and T axes with the principal stress axes $\mathbf{s}_1$, $\mathbf{s}_2$, and $\mathbf{s}_3$ if an angular error of $\varphi_0/2 \approx 15°$ is accepted (Figure 1c) [*Raleigh et al.*, 1972; *Molnar and Chen*, 1982; *Célérier*, 1988].

[16] The third premise that a principal stress direction is vertical near the Earth's surface restricts the state of stress to three tectonic regimes associated with specific types of faulting [*Anderson*, 1905]. In the extensional regime, $\mathbf{s}_1$ is vertical, faulting is purely normal (rake = −90°), the fault plane dips at φ_1, and the second nodal plane dips at φ_2 (Figure 3a). In the compressional regime, $\mathbf{s}_3$ is vertical, faulting is purely reverse (rake = +90°), the fault plane dips at φ_2, and the second nodal plane dips at φ_1 (Figure 3b). Sandbox modeling, using isotropic material, supports both cases [*Hubbert*, 1951]. In the first and second cases, the P and T axes should be at angle $\varphi_0/2 \approx 15°$ from the vertical, respectively. The symmetry that exchanges $\mathbf{s}_1$ with $\mathbf{s}_3$ also exchanges the fault plane with the auxiliary plane: the dip distribution of nodal planes should therefore be similar in both cases. In the wrench regime, $\mathbf{s}_2$ is vertical, faulting is purely strike slip (rake = 0° or 180°), and both nodal planes are vertical (Figure 3c).

2.2. Frictional Reactivation

[17] The simplest model to take the strength anisotropy from preexisting structures into account is probably that of frictional slip on a plane of weakness [*Wallace*, 1951; *Talobre*, 1957; *Bott*, 1959; *Jaeger*, 1959, 1960; *Handin*, 1969; *McKenzie*, 1969; *Byerlee*, 1978]. The friction law is identical to the Coulomb criterion (equation (1)), but the cohesion and friction coefficients are lower than those for new rupture, and the plane of weakness orientation is not necessary optimal.

[18] In this situation, the friction line intersects Mohr's outer circle instead of being tangent to it. This implies that a range of orientations of weak planes can be activated by the same state of stress, as opposed to a couple of conjugate planes in the case of rupture. Conversely, slip on a given fault plane can be due to a range of states of stress and therefore provides only a weak constraint on the principal stress orientations.

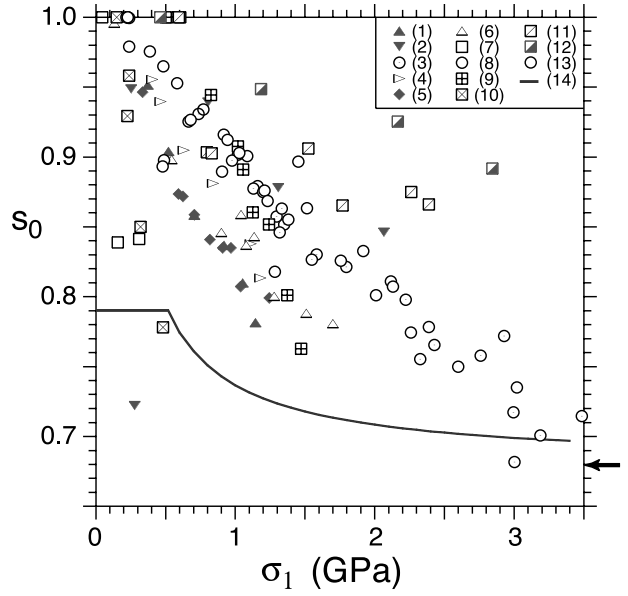

Figure 2. Normalized stress difference, s_0, required to generate a new fracture or to activate an optimally oriented preexisting fracture as a function of the maximum effective stress. New fracture generation in (1) Orikabe Diorite [*Mogi*, 1965], (2) Frederick Diabase [*Brace*, 1964], (3) Westerly Granite [*Byerlee*, 1967], (4) Mannari Granite [*Mogi*, 1965], (5) Haruyama Peridotite [*Mogi*, 1965], (6) Kitashirakawa Granite [*Matsushima*, 1959, 1960], (7) Marble [*Brace et al.*, 1966], (8) Westerly Granite [*Mogi*, 1966a, 1966b], (9) Blair Dolomite [*Brace*, 1964], (10) Webatuk Dolomite [*Brace*, 1964], (11) Aplite [*Brace et al.*, 1966], (12) Cheshire Quartzite [*Brace*, 1964], and (13) Westerly Granite [*Brace et al.*, 1966] and (14) reactivation of optimally oriented fracture with standard frictional properties as in equations (14) and (15) [*Byerlee*, 1978]. The small arrow to the bottom right indicates the high-pressure threshold, $s_c(\mu)$ (equation (6)), which is also applicable when cohesion is negligible. Data 1–13 are also found in the compilations of *Ohnaka* [1973] and *Sheorey* [1997].

[19] It is thus usual to rely on the assumption that the slip direction is parallel to the resolved shear stress on the reactivated plane, to further constrain the problem [*Schmidt and Lindley*, 1938; *Wallace*, 1951; *Bott*, 1959; *McKenzie*, 1969; *Célérier*, 1988, 1995]. *Bott* [1959] showed that the shear stress direction depends only on the principal stress orientation and the stress tensor aspect ratio

$$r_0 = \frac{\sigma_1 - \sigma_2}{\sigma_1 - \sigma_3}, \tag{11}$$

and *McKenzie* [1969] demonstrated that shear stress could be along the slip direction with principal stress orientations significantly away from, and even perpendicular to, the optimal stress orientations. This seriously undermines the relevance of optimal stress orientations in the case of reactivation.

[20] Yet the friction law restricts the range of orientations that can be activated with respect to a given system of principal stress directions. This range is controlled by the frictional parameters, τ_0 and μ, and by the state of stress parameters, s_0, r_0, and σ_1 [*Jaeger*, 1959, 1960; *Jaeger and Rosengren*, 1969; *Célérier*, 1988]. However, within the framework introduced in equations (1)–(11), three parameters are sufficient to discuss this control: μ, which controls the optimal orientations (Figure 1), and $s_0 - s_t(\mu, \tau_0, \sigma_1)$ and r_0, which control the extent around the optimal orientations.

[21] When $s_0 - s_t(\mu, \tau_0, \sigma_1) < 0$, no plane can be reactivated. When $s_0 - s_t(\mu, \tau_0, \sigma_1) = 0$, activation is possible on the optimal conjugate planes only. The only exception occurs if the intermediate stress magnitude equals either of the extreme stress magnitudes, i.e., $r_0 = 0$ or $r_0 = 1$. In that case the symmetry of the stress tensor defines a set of optimal planes that are tangent to a cone of revolution around the singular stress axis [*Wallace*, 1951; *Jaeger and Rosengren*, 1969; *Célérier*, 1988]. Reactivating nonoptimally oriented planes requires $s_0 - s_t(\mu, \tau_0, \sigma_1) > 0$, and the range of orientations that can be activated away from the optimal conjugate planes grows as $s_0 - s_t(\mu, \tau_0, \sigma_1)$ increases, as shown by two-dimensional analysis [*Jaeger*, 1959, 1960; *Sibson*, 1985]. Three-dimensional analysis adds the secondary possibility of further spreading this range in other directions when r_0 becomes close to 0 or 1 [*Jaeger and Rosengren*, 1969; *Célérier*, 1988].

2.3. Crustal Scenarios

[22] To apply this to crustal conditions, let us consider the fault frictional properties determined in the laboratory by *Byerlee* [1978] for most crustal rocks:

$$\tau = 0.85\,\sigma_n \quad \text{for} \quad \sigma_n \le 200\ \text{MPa} \tag{12}$$

$$\tau = 50 + 0.6\,\sigma_n \quad \text{for} \quad \sigma_n \ge 200\ \text{MPa}, \tag{13}$$

where τ is in MPa. The corresponding reactivation threshold, $s_t(\mu, \tau_0, \sigma_1)$, is obtained by combining equations (5) and (6) with equations (12) and (13):

$$s_t(\mu, \tau_0, \sigma_1) = s_c(\mu) = 0.79 \quad \text{for} \quad \sigma_1 \le 500\ \text{MPa} \tag{14}$$

and

$$s_t(\mu, \tau_0, \sigma_1) = 0.68 + \frac{56.66}{\sigma_1} \quad \text{for} \quad \sigma_1 \ge 500\,\text{MPa}, \tag{15}$$

where σ_1 is in MPa. Whether reactivation on optimal planes, on nonoptimal planes, or new fault creation occurs thus depends on where s_0 for crustal stress falls between this frictional bound, plotted as a line, and that for new failure, shown by symbols, on Figure 2. To address this question, let us consider first a standard scenario for fault properties and the state of stress and then significant variations.

[23] The standard scenario is that proposed by *Brace and Kohlstedt* [1980] where preexisting "standard faults," defined as those with the above frictional properties and submitted to hydrostatic pore pressure, span a sufficiently wide range of orientations to include those close to optimal

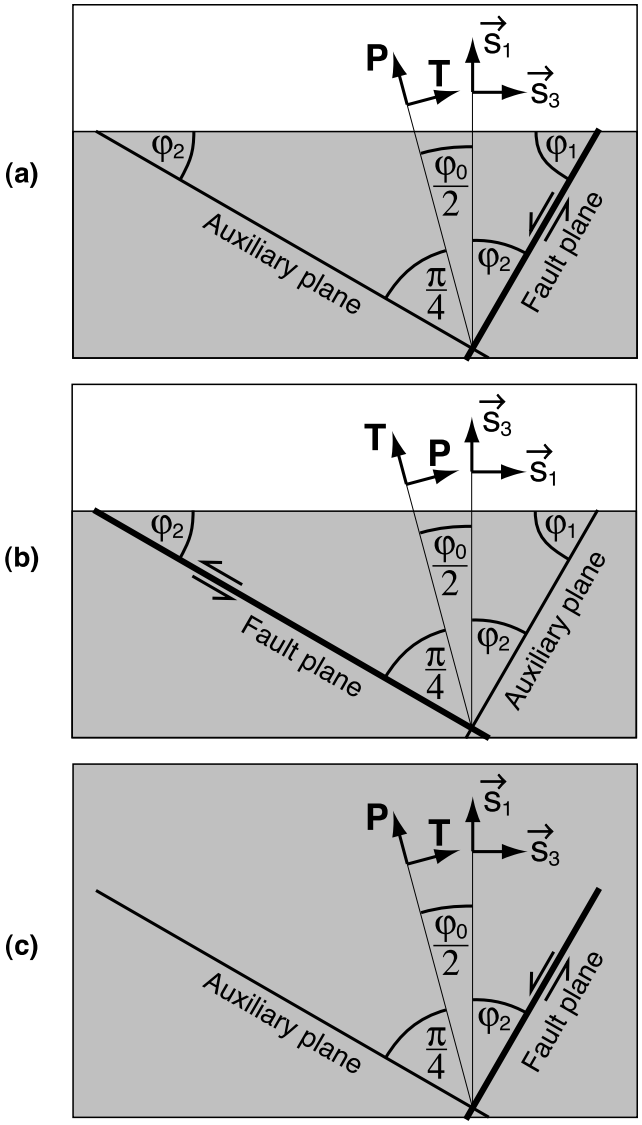

Figure 3. *Anderson*'s [1905] faulting geometry. Fault plane solution auxiliary plane and *P*, *B*, and *T* axes are also shown. Symbols are explained in Table 1. (a) Extensional regime. (b) Compressional regime. (c) Wrench regime. Figures 3a and 3b represent a vertical cross section whereas Figure 3c represents a map of the horizontal plane.

for any stress system. This scenario is then that of a fractured, yet isotropic, material where reactivation occurs on nearly optimal orientations as soon as s_0 reaches the threshold $s_t(\mu, \tau_0, \sigma_1)$ given by equations (14) and (15) [*Talobre*, 1957; *Jaeger*, 1962]. This threshold thus becomes the upper limit of s_0 for in situ stress with hydrostatic pore pressure [*Brace and Kohlstedt*, 1980; *Kohlstedt et al.*, 1995]. If we define "standard" stress conditions as those not only limited by this threshold but also with a vertical principal stress direction and with an intermediate stress magnitude significantly different from extreme stress magnitudes, then "standard" faults in these "standard" stress conditions will be reactivated only for orientations close to the optimal Andersonian conjugate planes [*Raleigh et al.*, 1972; *Célérier*, 1988]. This will be called "near"-Anderson faulting, and its geometry is thus indistinguishable from that of original Anderson faulting. Both cases will therefore be lumped together in the rest of this paper.

[24] The isotropy of this standard scenario can be broken down in two different ways. First, standard faults may not span enough orientations, so that preexisting optimal orientations may not be available. The stress difference may then rise above the frictional threshold, and nonoptimally oriented preexisting faults may be activated. If the preexisting faults are too severely misoriented, the stress difference may rise even further to reach the rupture threshold, and new optimal faults may be created. However, these new faults will be Andersonian if a principal stress direction remains vertical and the medium remains sufficiently isotropic.

[25] Second, a few orientations may correspond to faults with nonstandard properties due to either lower frictional parameters or local overpressures. In the first case, the reactivation threshold, $s_t(\mu, \tau_0, \sigma_1)$, is lower than that for standard faults (for example, $\tau_0 = 0$ and $\mu = 0.5$ gives $s_t(\mu, \tau_0, \sigma_1) = 0.54$, which is well below the standard curve shown on Figure 2). In the second case, $s_t(\mu, \tau_0, \sigma_1)$ remains that of equations (14) and (15), but s_0 can reach values up to 1 as pore pressure reaches the least total principal stress magnitude ($\sigma_3 = 0$). In both cases, the difference $s_0 - s_t(\mu, \tau_0, \sigma_1)$ may be large for the nonstandard fault even though it remains negative for nearby "standard" faults sustaining the same total stress. As a consequence, the nonstandard fault can be reactivated even if misoriented and thus appears weaker than the "standard" faults that remain stable. Conversely, the stress axes can be significantly away from the optimal directions deduced from the nonstandard fault attitude [*McKenzie*, 1969].

[26] Borehole stress measurements remain below the threshold of equations (14)–(15) and reach it in zones of active tectonics [*Zoback and Healy*, 1984; *Zoback et al.*, 1993; *Townend and Zoback*, 2000]. This supports the standard scenario and suggests that standard fault properties are ubiquitous, whereas nonstandard properties are restricted to a few orientations in a given region. This also suggests that values of s_0 above the threshold of equations (14)–(15) are more likely to be related to localized overpressures [*Rice*, 1992; *Sleep and Blanpied*, 1992], rather than to abnormally high regional stress difference.

[27] Determining how prevalent "near-Andersonian" faulting is in earthquake focal mechanisms is thus an alternate way of evaluating the relative importance of this standard scenario with respect to other conditions that include low friction coefficient, high stress difference, high pore pressure, or rotated stress axes.

3. RECOGNIZING ANDERSONIAN FAULTING IN FOCAL MECHANISMS

[28] The three types of Andersonian faulting have characteristic fault plane, slip, and principal stress orientations that can be recognized in the dip angles of the nodal planes, slip rake angles, and orientations of the *P*, *B*, and *T* axes of fault plane solutions.

3.1. Dips of Nodal Planes

[29] Normal and reverse faults, having complementary dip angles, exchange fault and auxiliary planes to yield the same values of dip, φ_1 and φ_2, when both nodal planes are considered together (Figures 3a and 3b). With "standard" friction values these angles become

$$\varphi_0 \approx 31^\circ, \tag{16}$$

$$\varphi_2 = \frac{\pi}{4} - \frac{\varphi_0}{2} \approx 30^\circ, \tag{17}$$

$$\varphi_1 = \frac{\varphi_0}{2} + \frac{\pi}{4} \approx 60^\circ. \tag{18}$$

[30] Nodal planes for strike-slip faulting are vertical. The relative abundance of these orientations can be estimated on histograms of nodal plane dips. Such histograms, however, present a geometrical bias due to the variation of the area covered by each interval on a sphere. To facilitate the interpretation, density-corrected histograms are superposed on the raw histograms. The applied correction is detailed in Appendix A.

3.2. Slip Rake

[31] Using *Aki and Richard*'s [1980, p.106] convention for orientation angles of nodal planes, normal and reverse faults yield rake angles of -90° and $+90^\circ$, respectively, whereas strike-slip faults yield rake angles of 0° and $\pm 180^\circ$. The abundance of these values can be directly estimated on histograms of slip rake angles.

3.3. *P*, *B*, and *T* Axes

[32] The *P*, *B*, and *T* axes are deduced from the optimal stress orientation, $\mathbf{s}_1$, $\mathbf{s}_2$, and $\mathbf{s}_3$, by a rotation of $\varphi_0/2 \approx 15^\circ$ around $\mathbf{s}_2$ (Figure 1c). Andersonian faulting is therefore expected to result in plunges of the *P* and *T* axes of $90 - \varphi_0/2 \approx 75^\circ$ and $\varphi_0/2 \approx 15^\circ$ in the case of normal faulting (Figure 3a) and of $\varphi_0/2 \approx 15^\circ$ and $90 - \varphi_0/2 \approx 75^\circ$ in the case of reverse faulting (Figure 3b). In both cases the *B* axis should be horizontal. For strike-slip faulting, the *P* and *T* axes should be horizontal, and the *B* axis should be vertical (Figure 3c).

[33] Plunge histograms of *P*, *B*, and *T* axes are therefore used to estimate the importance of Anderson faulting, as done before [*Bossu and Grasso*, 1996; *Bokelmann and Beroza*, 2000]. Density-corrected and raw histograms are superposed to facilitate interpretation as done for dip of nodal planes (Appendix A).

[34] The triangular representation introduced by *Frohlich* [1992], and detailed in Appendix B, is also used because it concentrates the information on the three plunges in a single diagram [*Frohlich and Apperson*, 1992; *Frohlich*, 1992, 2001]. It can be interpreted as representing the orientation of the vertical with respect to the *P*, *B*, and *T* frame of reference, as demonstrated in Appendix B. It is based on the gnomonic projection that does not conserve area, and we therefore rely on the histograms for density considerations and on the triangular representation for a synthetic view of the orientations of the axes. This diagram proves helpful when analyzing the relationship between vertical *P*, *B*, and *T* axes and pure dip-slip and pure strike-slip nodal planes. Such an analysis leads to two useful conclusions: (1) low *B* plunge is a better proxy for pure dip slip than high *P* or *T* plunge and (2) high *B* plunge is not a good proxy for pure strike slip (Appendix B).

3.4. Necessary but Not Sufficient Conditions

[35] Whereas Anderson faulting requires the conditions detailed in sections 3.1–3.3, they are not sufficient to ensure that faulting is Andersonian. Andersonian faulting means activation of optimal planes with a vertical principal stress direction. Verifying these two requirements requires determining fault and slip geometry and principal stress orientations.

[36] Whereas fault plane solutions do provide fault and slip orientation, albeit with the nodal plane ambiguity, the associated *P*, *B*, and *T* axes are reasonable proxies for the principal stress directions, with the $\varphi_0/2 \approx 15^\circ$ bias mentioned in section 2.1, only if the activated plane is close to optimal, which happens to be one of the clauses to verify. Overcoming this circular reasoning is possible in regional studies where the state of stress can be determined independently from the fault plane solution but is beyond the scope of the global analysis presented in this paper.

4. GLOBAL DATA SET

4.1. Initial Data Set

[37] The initial data set, CMT (Table 2), is the 1976 to 2004 Global Centroid Moment Tensor catalog that contains 22,477 events and is considered complete down to $M_w \geq 5.5$ [*Dziewonski et al.*, 1981; *Dziewonski and Woodhouse*, 1983; *Ekström et al.*, 2005].

4.2. Quality Criteria

[38] To obtain reliable orientations of the nodal planes and *P*, *B*, and *T* axes, the data are reduced to those that satisfy the three quality criteria proposed by *Frohlich and Davis* [1999] and applied to plate boundary tectonics analyses [*Frohlich and Apperson*, 1992; *Frohlich*, 2001]. These three criteria are (1) that all components are actually inverted for, (2) that the relative error of the moment tensor is sufficiently small, and (3) that the double couple component is dominant. To obtain orientation angular uncertainties around $5-10^\circ$ these requirements become [*Frohlich and Davis*, 1999]

$$n_{\text{free}} = 6, \tag{19}$$

$$E_{rel} \leq 15\%, \tag{20}$$

$$|f_{clvd}| \leq 0.2, \tag{21}$$

TABLE 2. Data Sets and Selection Ratios

Initial Data Set With Depth Range (km)	Number of Data	Selection Criteria[a]	Selected Data Set With Depth Range (km)	Number of Data	Ratio
		Depth			
CMT[b]	22,477	DR	CMT 0–30	6,355	28%
CMT[b]	22,477	DR	CMT 30–40	8,018	36%
CMT[b]	22,477	DR	CMT 40–300	6,798	30%
CMT[b]	22,477	DR	CMT 300–700	1,306	6%
		Quality			
CMT[b]	22,477	FD	FD	10,709	48%
CMT 0–30	6,355	FD+DR	FD 0–30	2,685	42%
CMT 30–40	8,018	FD+DR	FD 30–40	3,619	45%
CMT 40–300	6,649	FD+DR	FD 40–300	3,609	53%
CMT 300–700	1,455	FD+DR	FD 300–700	796	61%
		Rake: One Nodal Plane			
FD 0–30	2,685	FD+DR+R1P	FD 0–30 R1P	528	20%
FD 0–30	2,685	FD+DR+S1P	FD 0–30 S1P	1,130	42%
FD 0–30	2,685	FD+DR+N1P	FD 0–30 N1P	217	8%
FD 0–30	2,685	FD+DR+ (R1P*S1P*N1P)	total strike slip or dip slip on one plane	1,875	70%
		Rake: Both Nodal Planes			
FD 0–30	2,685	FD+DR+R2P	FD 0–30 R2P	267	10%
FD 0–30	2,685	FD+DR+S2P	FD 0–30 S2P	437	16%
FD 0–30	2,685	FD+DR+N2P	FD 0–30 N2P	147	5%
FD 0–30	2,685	FD+DR+ (R2P*S2P*N2P)	total strike slip or dip slip on both planes	851	32%
		Rake: One Versus Both Nodal Planes			
FD 0–30 R1P	528	FD+DR+R2P	FD 0–30 R2P	267	51%
FD 0–30 S1P	1,130	FD+DR+S2P	FD 0–30 S2P	437	39%
FD 0–30 N1P	217	FD+DR+N2P	FD 0–30 N2P	147	68%
Total strike slip or dip slip on one plane	1,875	FD+DR+ (R2P*S2P*N2P)	total strike slip or dip slip on both planes	851	45%

[a]FD, *Frohlich and Davis* [1999] quality criteria; DR, depth range selection; R1P, rake on one nodal plane within 10° of pure reverse (+90°); R2P, rake on both nodal planes within 10° of pure reverse (+90°); S1P, rake on one nodal plane within 10° of pure strike slip (0° or 180°); S2P, rake on both nodal planes within 10° of pure strike slip (0° or 180°); N1P, rake on one nodal plane within 10° of pure normal (−90°); N2P, rake on both nodal planes within 10° of pure normal (−90°). For combinations, "and" is denoted by pluses, and "or" is denoted by asterisks.

[b]CMT, the Global Centroid Moment Tensor catalog for the time period 1976–2004. The depth range is 0–700 km.

with

$$\|\mathbf{M}\| = \sqrt{\sum_{i=1}^{3}\sum_{j=1}^{3} m_{ij}^2}, \tag{22}$$

$$\|\mathbf{DM}\| = \sqrt{\sum_{i=1}^{3}\sum_{j=1}^{3} dm_{ij}^2}, \tag{23}$$

$$E_{rel} = \frac{\|\mathbf{DM}\|}{\|\mathbf{M}\|}, \tag{24}$$

$$f_{clvd} = -\frac{m_B}{\max(|m_P|, |m_T|)}, \tag{25}$$

where **M** is the moment tensor; **DM** is its standard error; m_P, m_B, and m_T are its eigenvalues; and n_{free} is the number of actually inverted components.

[39] The first condition (equation (19)) is particularly relevant to this analysis. Close to the surface, two components of the moment tensor are often too poorly constrained to be inverted for and are instead arbitrarily set to zero. This results in a moment tensor with a vertical principal axis and either in pure dip-slip focal mechanisms (rake = ±90°) with 45° dipping nodal planes or in pure strike-slip mechanisms (rake = 0° or 180°) with vertical nodal planes. These artifacts could be misinterpreted as Andersonian faults, even if, in the dip-slip cases, the dip of the nodal planes would suggest negligible friction.

4.3. Reduced Data Set

[40] Extracting the data that satisfy the three quality criteria of equations (19)–(21) from the CMT data set yields the 10,709 event data set labeled FD (Table 2). The data reduction is about 48% on average and decreases with depth: it varies from 42% for shallow data up to 61% for deep data (Table 2, sixth column). This bias remains small and the depth distribution remains reasonably representative of the initial data set (Figure 4).

[41] The rake distribution of the FD data set shows four modes (Figure 5a). The major mode, +90°, corresponds to pure reverse faulting and is more than twice as large as the next modes. The three minor modes have similar magnitude and correspond to pure strike-slip (0° and ±180°) and pure normal (−90°) faulting. The four distribution minima are about one third of the minor mode magnitude and occur for oblique slip at 45° from the modes.

[42] The raw distribution of dips of nodal planes is widely spread with a deficit in the 0–15° range. This deficit is compensated by the density correction (Appendix A) that reveals a 15–25° mode (Figure 5b).

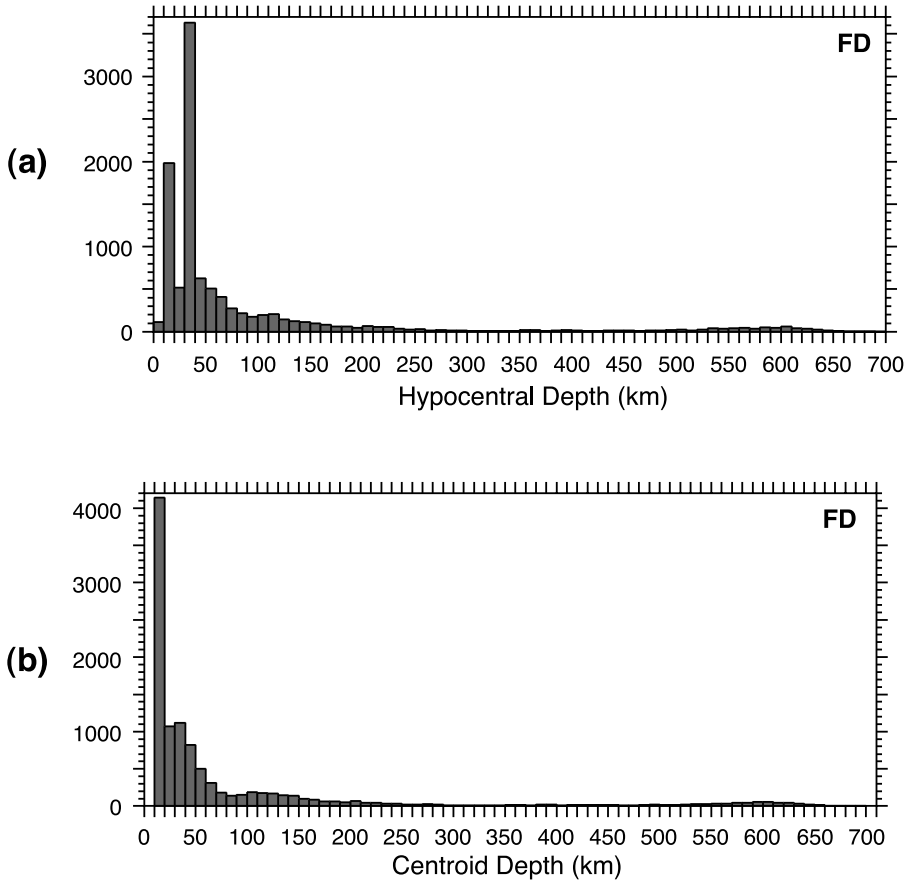

Figure 4. FD data set (10,709 events, Table 2), satisfying the quality requirements [*Frohlich and Davis*, 1999]. (a) Hypocenter depth and (b) centroid depth.

[43] The plunge distributions of the *P*, *B*, and *T* axes are bimodal with a shallow and steep mode, except for that of the raw *P* axes that has a shallow mode only (Figures 5c–5e). The shallow mode is horizontal for the *B* and *T* axes and spreads over 0–25° for the *P* axes. The steep mode is sensitive to the density correction: it is shifted from 65–70° to 65–75° for the raw and corrected *T* axis plunge and from 70–80° to 85–90° for the raw and corrected *B* axis plunge, and it appears at 80–90° in the corrected data only for the *P* axis plunge.

4.4. Interpretation

[44] The clear preference for pure dip slip and strike slip shown in the rake distribution is surprising given the diversity of geodynamic conditions integrated in this global data set. However, this consistency quickly reaches its limits: whereas a significant contribution of Andersonian mechanisms would result in similar rake modes, it would produce different dip distributions of nodal planes and plunge distributions of the *P* and *T* axes. Further analysis therefore requires separating the diverse geodynamic settings and, in particular, subduction and nonsubduction related events.

5. DEPTH ANALYSIS

[45] A first-order separation aims to isolate those crustal events more likely to succumb to the Andersonian temptation from subduction zone events more likely to be influenced by the dipping slab geometry. A 40 km lower limit, which is shallower than the traditional 70 km limit for shallow earthquakes and may exclude a few rare lower crustal events in orogenic belts, is chosen because it better focuses on near-surface events. These shallow events are subdivided into 0–30 km and 30–40 km intervals because of two considerations. First, this yields two intervals with similar amounts of data and gives a chance to identify a possible variation with depth of the influence of a vertical principal stress. Second, this allows the isolation from the upper 0–30 km interval of the significant number of poorly constrained hypocenter depths set at 33 km (Figure 5a) that may correspond to deeper mislocated events.

[46] The change from reverse to normal in the dominant faulting mode of deeper events with increasing depth suggests a separation of the data at the 300 km boundary commonly used to distinguish intermediate (70–300 km) from deep focus (>300 km) earthquakes. The data are thus sorted into four depth intervals, 0–30, 30–40, 40–300, and 300–700 km (Table 2), on the basis of hypocenter depth, assumed to be more representative of the rupture initiation location than centroid depth.

5.1. Deep Events: 300–700 km

[47] The data within the 300–700 km depth range are localized exclusively in subduction zones, as expected

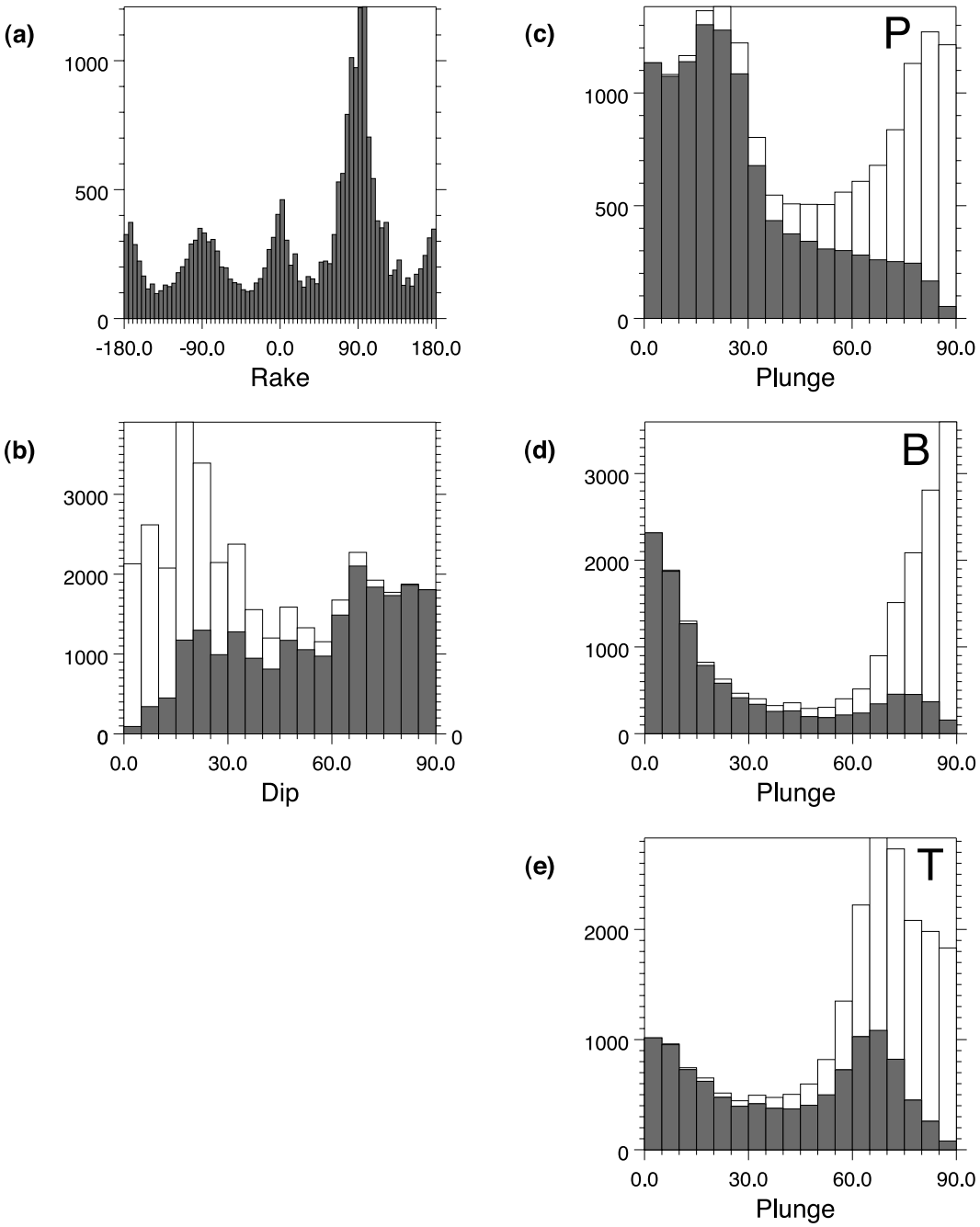

Figure 5. FD data set (10,709 events, Table 2). (a) Rake and (b) dip histograms of both nodal planes together. (c) *P*, (d) *B*, and (e) *T* axis plunge histograms. The top of the solid rectangles outlines the raw histograms whereas that of the hollow rectangles outlines histograms corrected for density as explained in Appendix A. Rake follows *Aki and Richards*'s [1980, p. 106] convention. Because both nodal planes are considered, the number of data in Figures 5a and 5b is twice that in Figures 5c–5e.

(Figure 6a). The rake distribution is dominated by a normal faulting mode (Figure 6b). The frequency of other slip rakes is around a third of that mode except that of sinistral slip. The sinistral slip frequency is half that of dextral slip, which is intriguing, even if the small number of events does not preclude statistical undersampling. Because strike-slip events with steeply dipping nodal planes yield both a sinistral and a dextral slip, the origin of this imbalance is to be found in events combining a low-dip strike-slip and a high-dip oblique-slip nodal plane. Above 500 km such events with dextral and sinistral slip roughly balance each other. But below that depth, the dextral events, mostly located in the Tonga subduction zone, dominate.

[48] The horizontal *B* axis mode (Figure 6f) reflects the dip-slip rake mode. The *P* and *T* axis plunge distributions are widely spread with weak modes around 40–60° and 20–40°. The wide scatter of the triangular representation illustrates the importance of oblique axes (Figure 6d). The

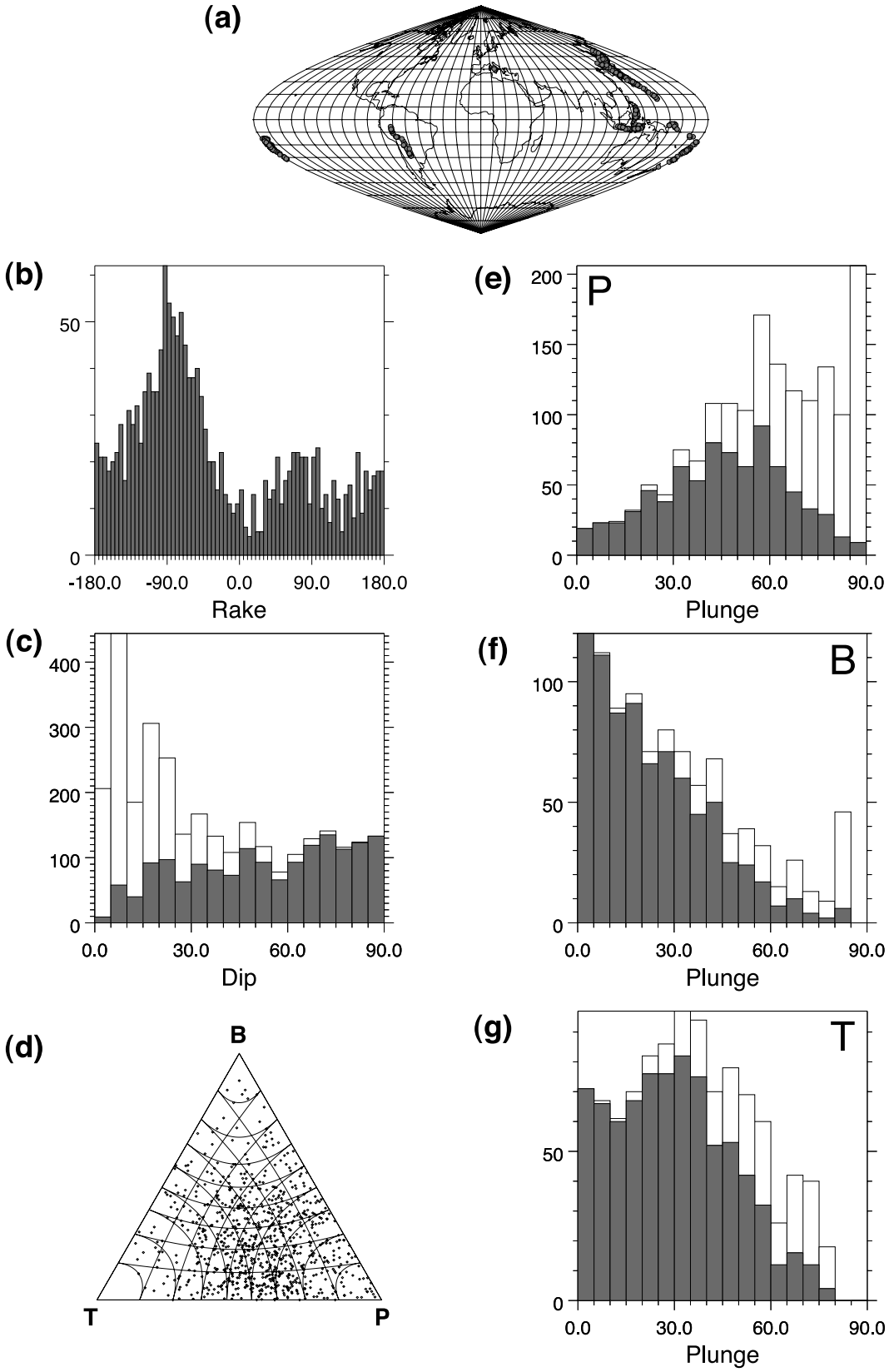

Figure 6. The FD 300–700 data set with hypocentral depth within the 300–700 km range (796 events, Table 2). (a) Epicenter map. Sanson-Flamsteed sinusoidal equal area projection [*Snyder*, 1987]. Latitude and longitude grid drawn every 10°. (b) Rake and (c) dip of both nodal planes together. (d) Triangular representation of the orientation of the vertical with respect to the *P*, *B*, and *T* axes [*Frohlich*, 1992, 2001] (Appendix B). (e) *P*, (f) *B*, and (g) *T* axis plunge histograms. The top of the filled rectangles outlines the raw histograms whereas the top of the hollow rectangles outlines the dip or plunge-corrected histograms (the correction is explained in Appendix A).

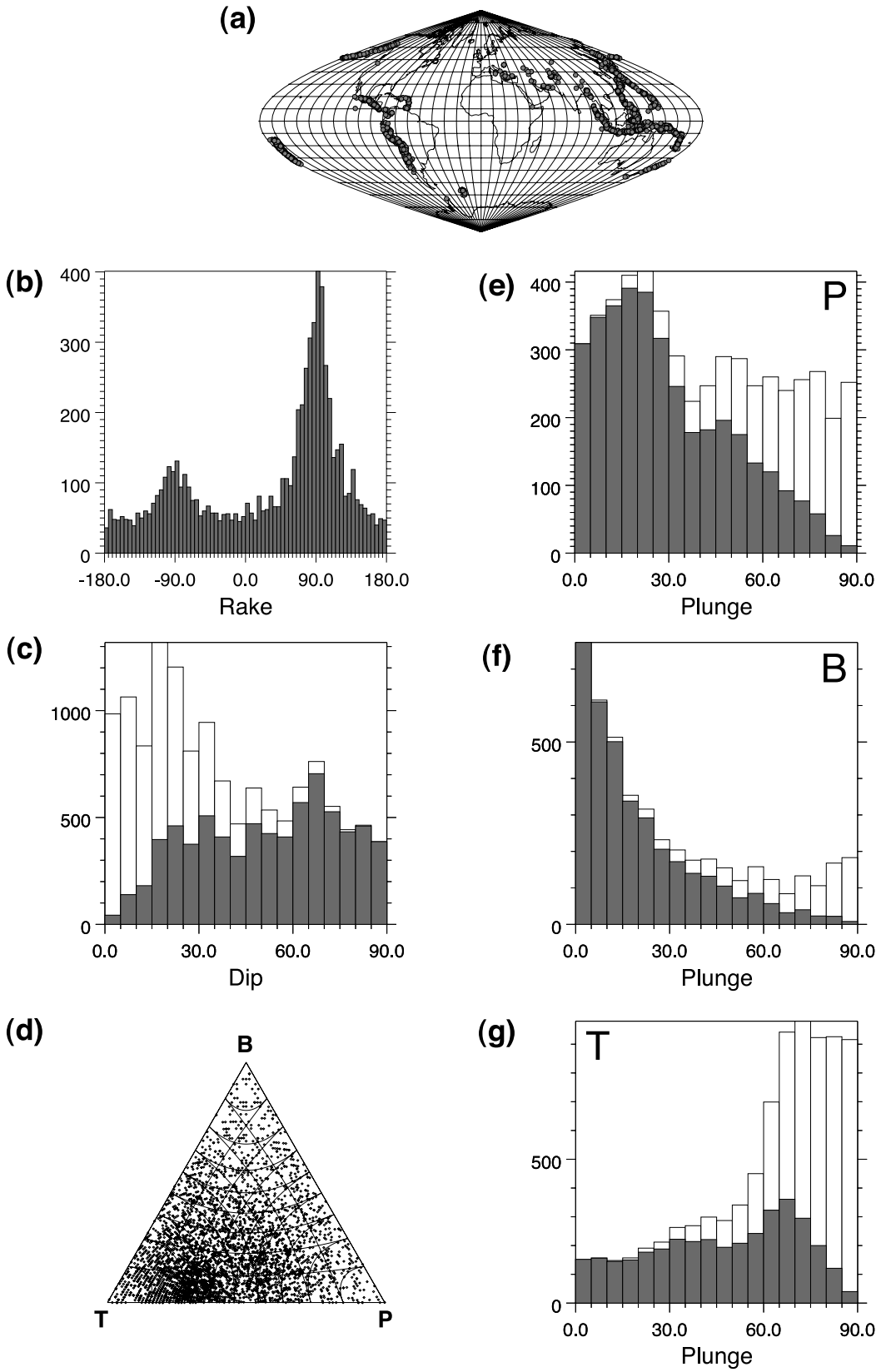

Figure 7. The FD 40–300 data set with hypocentral depth within the 40–300 km range (3609 events, Table 2). Same conventions as in Figure 6.

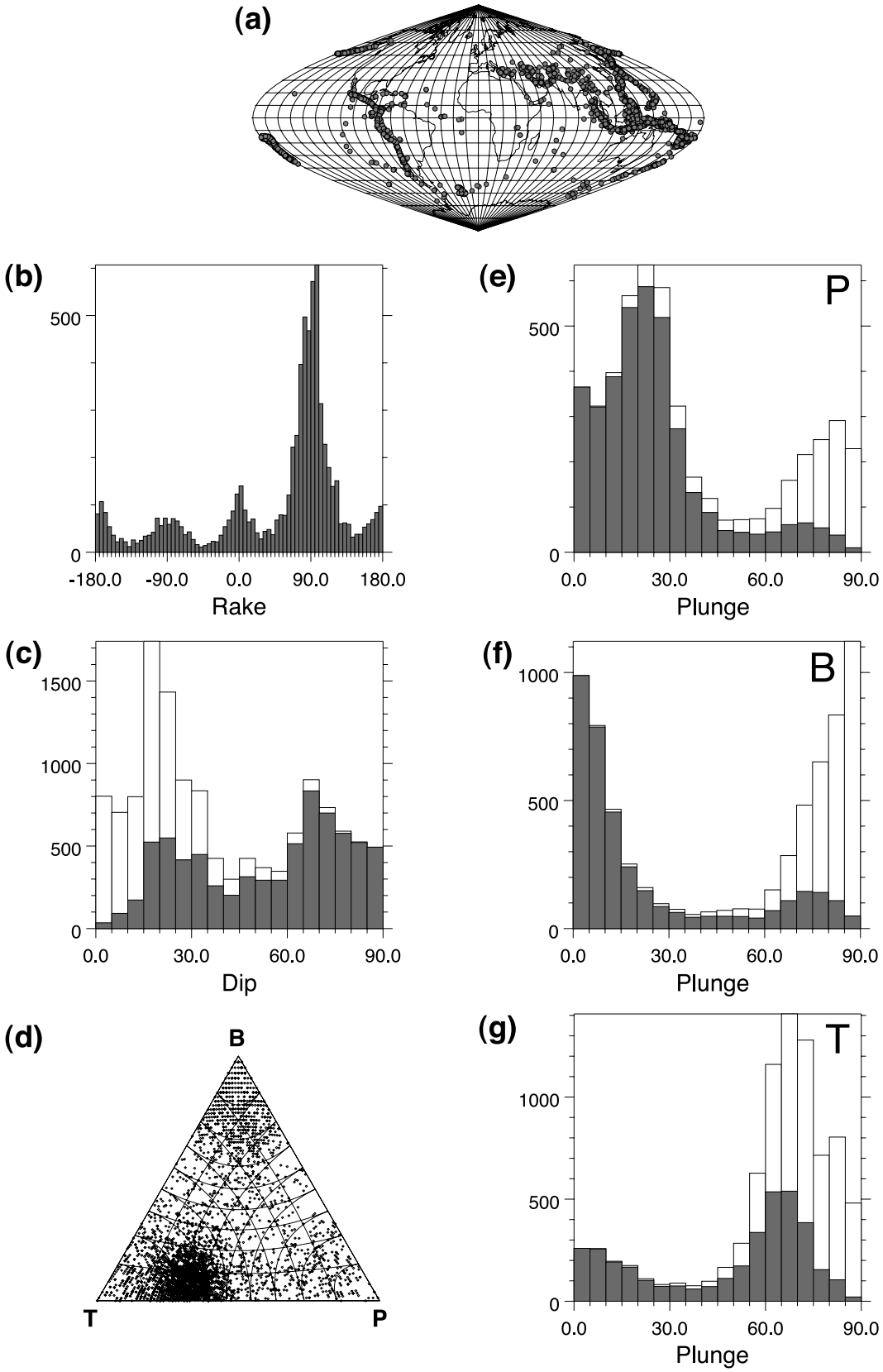

Figure 8. The FD 30–40 data set with hypocentral depth within the 30–40 km range (3619 events, Table 2). Same conventions as in Figure 6.

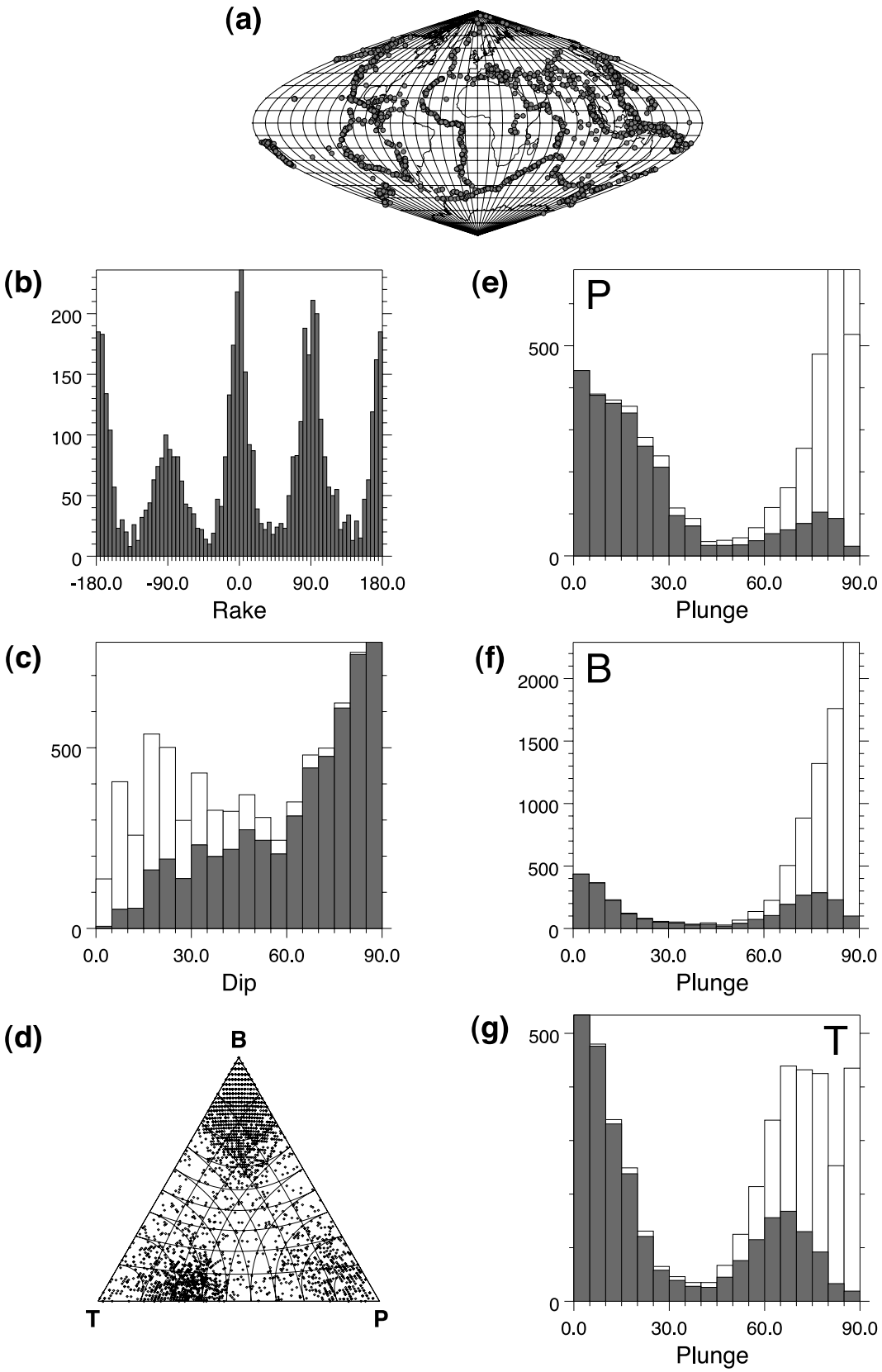

Figure 9. The FD 0–30 data set with hypocentral depth within the 0–30 km range (2685 events, Table 2). Same conventions as in Figure 6.

raw distribution of the nodal plane dip is wide with a slight low-dip deficit. The density correction compensates for this deficit and reveals a 5–10° mode (Figure 6c).

5.2. Intermediate Events: 40–300 km

[49] Seismicity in the 40–300 km depth interval is located mainly along subduction zones but also within continental convergence zones (Figure 7a). The orientation parameters from this interval show significant differences from those from the 300–700 km interval.

[50] The slip rake is dominated by a reverse faulting mode, with a secondary normal faulting mode about three times smaller (Figure 7b). Strike-slip faulting has about the same frequency as any oblique faulting: about an eighth of the major mode. The strong horizontal mode of the *B* axes (Figure 7f) is consistent with the dip-slip modes (Figure 7b). The raw distributions of the *P* and *T* axis plunges are widely spread with weak modes around 15–25° and 60–75°, respectively (Figures 7e–7g). The corrected distributions show two steps, with the high step at 10–30° and 65–90° for *P* and *T* axes, respectively. Oblique axes with various orientations are also well represented by the dispersion of the data in the triangular diagrams (Figure 7d).

5.3. Interpretation of Deep and Intermediate Events

[51] The distribution modes and dispersion described in sections 5.1 and 5.2 are consistent with the typical subduction system, with subhorizontal *B* axes and either of the *P* or *T* axes along the slab dip direction, as well as with the numerous deviations from this typical system, reported since the first focal mechanisms studies of subduction zones [*Isacks and Molnar*, 1969, 1971; *Apperson and Frohlich*, 1987; *Chen et al.*, 2004]. The shift from normal to reverse dominated mechanisms between deep and intermediate events is also consistent with the general downdip compression for the deep events and the mixed downdip extension and compression for the intermediate events detailed in the same studies. This effect may be reinforced by the decrease of slab dip from 40–70° below 125 km to 10–40° above it [*Lallemand et al.*, 2005] because downdip compression along a low-dip slab will produce reverse events. The smaller rotation of the *P* and *T* axis modes from the horizontal or vertical directions for the intermediate events with respect to the deep events can also be attributed to this slab dip decrease.

5.4. Shallow Events: 30–40 km

[52] The data from the 30–40 km depth interval are located in various tectonic settings that are not restricted to convergence zones (Figure 8a). The slip rake distribution has four modes, each corresponding to pure dip slip or strike slip (Figure 8b). The pure reverse mode is about five times larger than the next strike-slip modes, and the smallest mode corresponds to pure normal slip. The frequency is minimal for oblique slips at 45° from the modes where it is less than a tenth of the major reverse mode.

[53] The distributions of the plunges of the *P*, *B*, and *T* axes are bimodal with a shallow and steep mode (Figures 8e–8g). The *B* axis horizontal mode reflects the dip-slip rake modes. Its steeper mode around 70–80° in the raw data becomes vertical after density correction. The *P* axis major mode is 15–30° from the horizontal, and its minor mode ranges from 70 to 75° for the raw data to 80–85° for the corrected data. The *T* axis minor mode is horizontal, and its major mode is 60–75°. The triangular diagram with few scattered data in the center confirms the trend for the vertical to be close to one of the three axes (Figure 8d). Nodal plane dips are weakly bimodal with modes at 15–25° from the horizontal and the vertical (Figure 8c).

5.5. Shallow Events: 0–30 km

[54] The 0–30 km depth interval includes various tectonic settings like the previous 30–40 km interval but with the notable addition of mid-oceanic ridge events (Figure 9a). The rake distribution has four modes: three major modes of similar magnitudes, sinistral, dextral, and reverse, and one minor normal mode that is about half the major modes (Figure 9b). Frequency is minimal for oblique slip at 45° from pure dip slip or strike slip where it is less than a tenth of the major modes. Comparing the frequencies with that of an equivalent uniform distribution, which is 75 for a 5° bin, highlights a deficit in oblique slips: the four minima are about five times smaller than this yardstick, whereas the three major modes are two and a half to three times larger, and the minor mode is about a third larger.

[55] The distributions of the plunges of the *P*, *B*, and *T* axes are bimodal with a horizontal and a steep mode (Figures 9e–9g). The major mode is horizontal for the raw data but becomes vertical after density correction for *P* and *B*. The *P* and *B* steep modes are around 75–80° for the raw data but become vertical after density correction. The *T* steep mode is around 65–70° for the raw data and spreads within 65–90° after density correction. This strongly bimodal distribution of the *P*, *B*, and *T* axis plunges is confirmed by the triangular diagram with only sparse data in the central region (Figure 9d). A vertical mode in the nodal plane dip distribution (Figure 9c) distinguishes this depth interval from all deeper intervals.

5.6. Interpretation of Shallow Events

[56] Three major differences distinguish the shallow events from the deeper events: strike-slip rake modes, very low rake minima for oblique slips at 45° from strike or dip, and strong vertical and horizontal plunge modes of the *P*, *B*, and *T* axes. This, together with the pure dip-slip rake modes, is consistent with the idea that near-Andersonian conditions dominate the distribution, without discounting the importance of other conditions expressed by the significant nonmodal values of the distributions.

[57] This trend is less marked within 30–40 km than within 0–30 km. This is consistent with the expectation that these conditions are best expressed near the surface where the vertical is most likely to be close to a principal stress direction. However, it may also be due to the fact that many events with poorly constrained depth within the 30–40 km interval may actually be deeper and give this interval some attributes of deeper intervals.

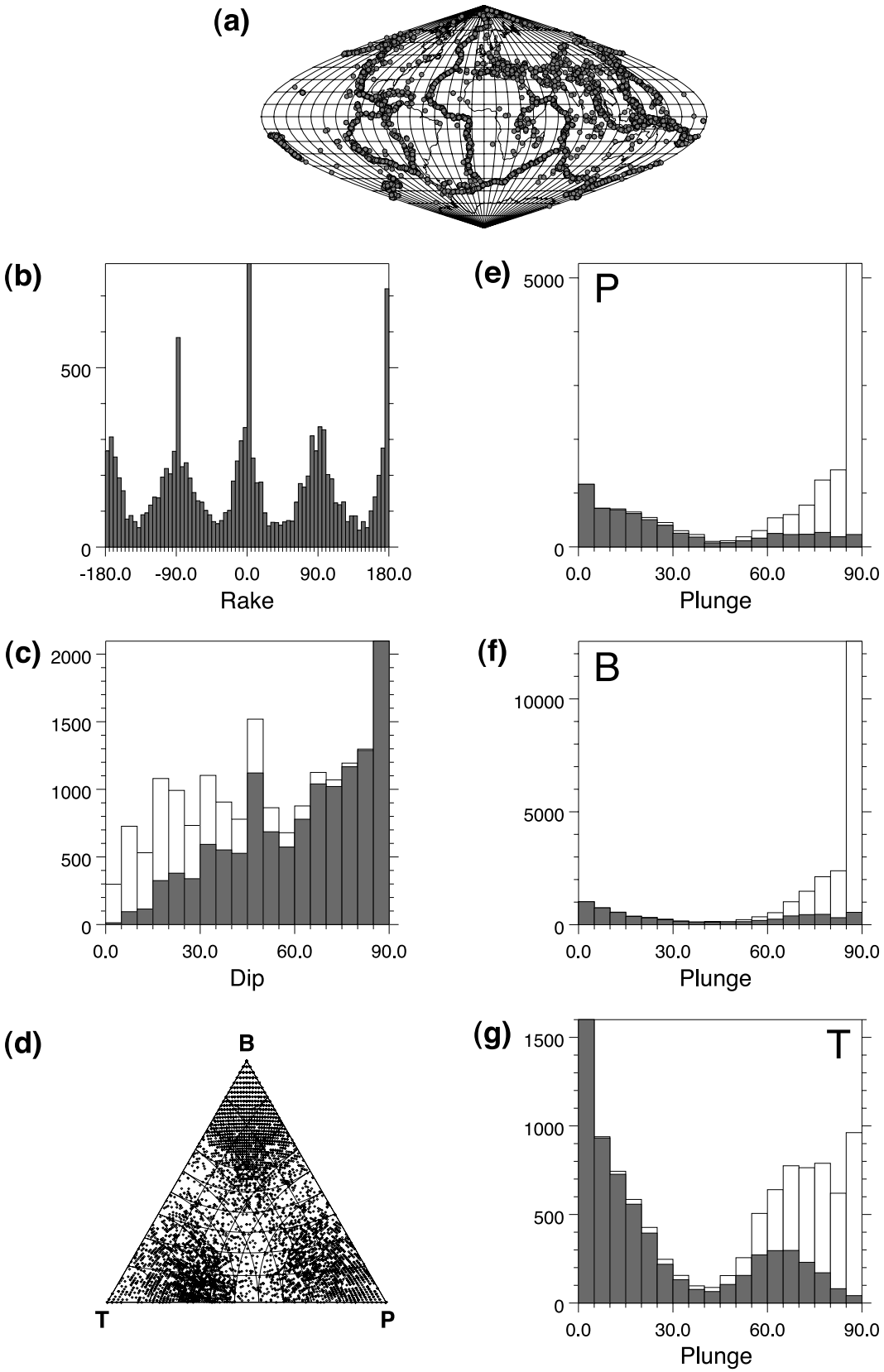

Figure 10. The CMT 0–30 data set with hypocentral depth within the 0–30 km range (6355 events, Table 2). Same conventions as in Figure 6.

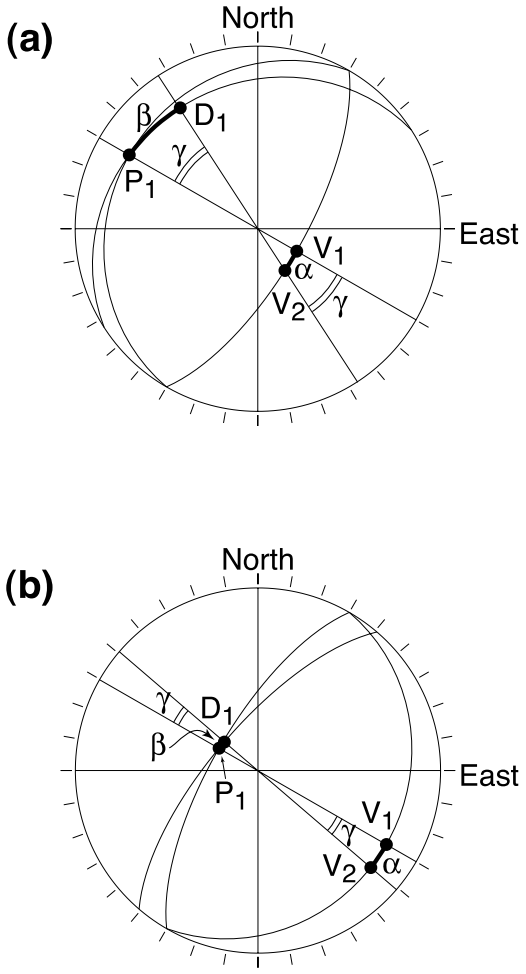

Figure 11. Pure and near-dip-slip nodal plane and corresponding second nodal plane. The pure dip-slip nodal plane pole is P_1, and its slip direction is along V_1; its associated second nodal plane pole is V_1, and slip direction is P_1. The near-dip-slip nodal plane pole is P_1, and its slip is along V_2; its associated second nodal plane pole is V_2, and slip direction is P_1. The dip direction within this second plane is labeled D_1. The angles between V_1 and V_2 and P_1 and D_1 are named α and β, respectively. The central angle bounded by P_1 and D_1 and by V_1 and V_2 is named γ. (a) Case where the first nodal plane has a steep dip. (b) Case where the first nodal plane has a shallow dip.

5.7. Selected Versus Complete Data Set

[58] The effect of the selection process is best assessed in the 0–30 km interval, not only because this is where Andersonian conditions dominate but also because this is where the selection is the most stringent with only 42% of retained data (Table 2). The full data set, CMT 0–30, distributions of rake, nodal plane dips, and plunges of the *P*, *B*, and *T* axes are shown on Figure 10.

[59] The most obvious difference between the selected (Figure 9) and the full data set (Figure 10) is the elimination of a significant number of pure dip-slip or pure strike-slip rakes, of 45° and 90° nodal plane dips, and of horizontal and vertical *P*, *B*, and *T* axes. This difference can be attributed to the elimination of moment tensors with arbitrarily imposed naught components at shallow depth (equation (19)).

[60] A more subtle effect of the selection is indicated by a similarity rather than by a difference between the two rake distributions. The minima at oblique rakes at 45° from pure strike or dip slip are about a tenth of the highest modes in both cases. This happens despite the fact that the modes are reduced by about a factor of three in the selected data. The selection is therefore also reducing these oblique slips by a factor of three. This means many oblique slips in the full data set do not meet the requirement either of low error (equation (20)) or of high double couple component (equation (21)). The preference for slip to be close to dip or strike direction is thus enhanced in well-constrained data, as shown by the reduction of the number of events located near the center of the triangular diagrams (Figure 9d versus 10d).

6. DIP-SLIP OR STRIKE-SLIP EVENTS

[61] The distributions of rake and plunges of the *P*, *B*, and *T* axes clearly suggest a dominant contribution of Andersonian mechanisms in the shallow (0–30 km) seismicity (Figure 9). However, although the wrench regime is well represented in the nodal plane dip distribution by a vertical mode, the 30° and 60° modes of the compressional and extensional regimes are not found. Furthermore, the *P* and *T* axis steep plunge modes are not similar, contrary to what is expected from Anderson normal and reverse faulting. These discrepancies may in part be due to the mixing of Andersonian with non-Andersonian events.

[62] This suggests isolating the three types of Andersonian faulting to characterize their geometry. As mentioned before, we can only rely on necessary conditions to try and identify these events. Selecting on the basis of the plunges of the *P*, *B*, and *T* axes is not straightforward, as mentioned before and detailed in Appendix B (Figure B1). Selecting on the basis of nodal plane dip or plunges of the *P*, *B*, and *T* axes would require an estimate of friction angles (Figure 3). Selecting on the basis of rake is simple, can directly be applied to the raw data, and allows the use of the resulting plunges of the *P*, *B*, and *T* axes and nodal dips to infer the fault frictional properties. The choice is thus easily made to isolate pure dip-slip and pure strike-slip mechanisms.

6.1. Method

[63] A first approach is to select within the FD 0–30 km data set events with at least one nodal plane with slip rake within 10° of pure reverse, normal, or strike slip and isolate them into three data sets. This approach yields a reasonable amount of data for each type of faulting (Table 2).

[64] However, this does not guarantee that the actual fault plane slip is within 10° of pure strike slip or dip slip because it may correspond to the nodal plane other than that which justified the selection. How much the alternate nodal plane rake may vary can be assessed on stereographic projection after distinguishing the two cases where the selected slip is close to the dip or to the strike direction.

[65] In the dip-slip case, let us consider two events with the same first nodal plane of pole P_1 but with two different slip vectors: one, V_1, exactly along dip and the other, V_2, at

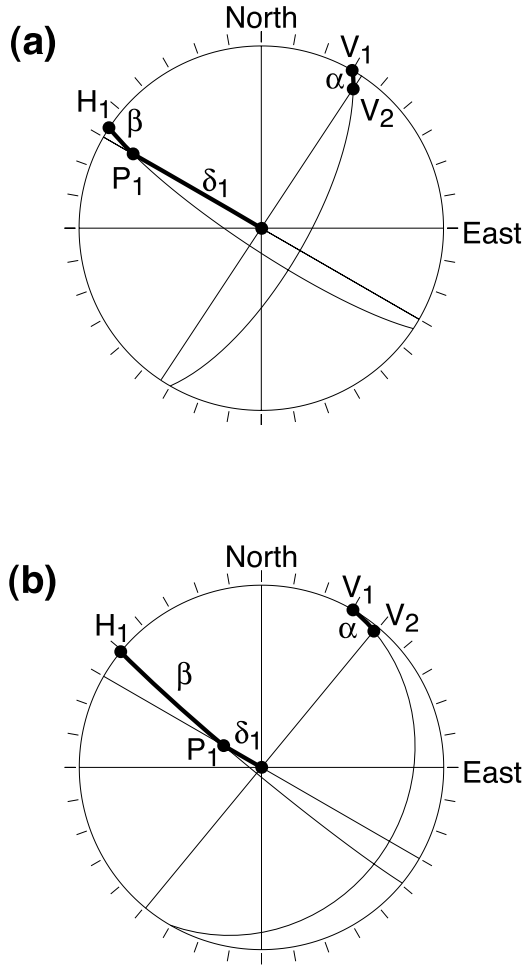

Figure 12. Pure and near-strike-slip nodal plane and corresponding second nodal plane. The pure strike-slip nodal plane pole is P_1, and its slip direction is along V_1; its associated second nodal plane pole is V_1, and slip direction is P_1. The near-strike-slip nodal plane pole is P_1, and its slip is along V_2; its associated second nodal plane pole is V_2, and slip direction is P_1. The horizontal direction within this second plane is labeled H_1. The angles between V_1 and V_2 and P_1 and H_1 are named α and β, respectively. The first nodal plane dip angle is named δ_1. (a) Case where the first nodal plane has a steep dip. (b) Case where the first nodal plane has a shallow dip.

small rake angle, α, from pure dip (Figure 11). The pole and slip direction of the second nodal plane for each event is obtained by exchanging those of the first nodal plane. The pure dip-slip event thus corresponds to a pure dip-slip second nodal plane of pole V_1 and slip P_1. The other event corresponds to a second nodal plane with pole V_2 and slip P_1. Let us call D_1 the downdip direction within this second plane and β the rake angle between P_1 and D_1. The angles α and β, measured within each nodal plane, are linked by the same dihedral angle, γ, between the two vertical planes than contain the pole, V_2, and the slip, P_1, respectively. This dihedral angle is also the central angle in stereographic projection. This geometry implies that if the dip of the first nodal plane is steep, then that of the second nodal plane is shallow, and β is larger than α (Figure 11a). Conversely, if the dip of the first nodal plane is shallow, that of the second nodal plane is steep, and β is smaller than α (Figure 11b). In other words, an event with near dip slip and steeply dipping first nodal plane may correspond to a second nodal plane with a significant strike-slip component.

[66] In the case of a near-strike-slip mechanism, the two considered events also share the same first nodal plane of pole P_1 with different slip vectors: one, V_1, exactly along strike and the other, V_2, at small rake angle, α, from pure strike (Figure 12). Let us call δ_1 the first nodal plane dip. The pure strike-slip event corresponds to a vertical second plane with a slip vector along P_1 plunging at $90^\circ - \delta_1$. The other event second nodal plane is steeply dipping because its pole, V_2, has a shallow plunge. The rake difference, β, between the slip vector, P_1, and pure strike slip, H_1, remains close to the plunge of P_1, that is, to $90^\circ - \delta_1$. The conclusion is the reverse of that for dip-slip events: a near-strike-slip shallow dip first nodal plane may correspond to a second nodal plane with a significant dip-slip component (Figure 12b).

[67] Hence, selecting slip orientation close to dip or strike on one nodal plane may include a second nodal plane with significant oblique slip depending on the first nodal plane dip. Slip can then be required to be close to pure strike slip or dip slip either on at least one of the nodal planes by a loose constraint or on both of the nodal planes by a strict constraint. Each approach has its advantages and drawbacks: in the first case, actual oblique slip events may be included in the selection, whereas in the second case, actual pure dip-slip or strike-slip events may have been discarded from the selection. The results of both methods are therefore presented and labeled as 1P and 2P for one and two planes slip requirement, respectively (Table 2). In both cases, rake is required to be within 10° of pure dip slip or strike slip. Globally, the strict method, 2P, culls 55% of the data retained by the loose method, 1P. The above discussion is thus relevant to a significant proportion of events.

6.2. Reverse 0–30 km

[68] Reverse events represent between 20% (R1P) and 10% (R2P) of the 0–30 km data (Table 2). This is about two to three times the 6% ratio of the 20° rake selection sector to the total rake range. Most events are located in convergence zones, but a few are near mid-oceanic ridges (Figures 13a and 14a).

[69] The B axis is subhorizontal with $0-10^\circ$ plunge (Figures 13f and 14f), as required for slip to be along the dip direction. The plunge distributions of the P and T axes are unimodal with a shallow, but not horizontal, P mode around $20-30^\circ$ and steep, but not vertical, T mode around $60-90^\circ$ (Figures 13e–13g and 14e–14g and Table 3). The steep T axis plunge mode is very sensitive to the density correction that shifts it from $60-65^\circ$ to $85-90^\circ$. In the triangular diagram, these orientations are located in a band along the P-T edge with a cluster at $20-30^\circ$ from the T vertex (Figures 13d and 14d).

[70] The R2P data set retains only 51% of the R1P set (Table 2). The two corresponding distributions are more

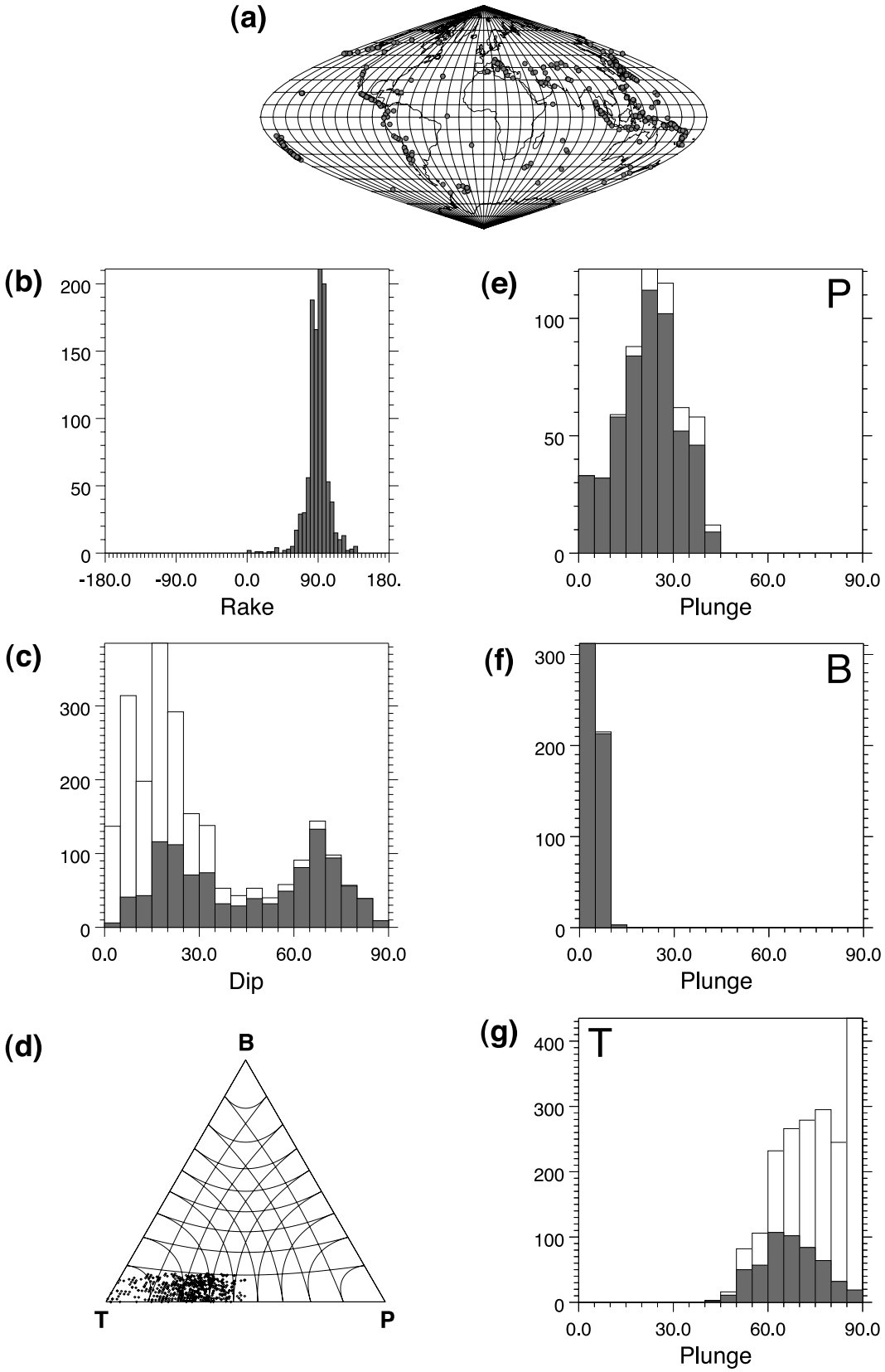

Figure 13. The FD 0–30 R1P data set with depth within the 0–30 km range and with rake within 10° of pure reverse for at least one nodal plane (528 events, Table 2). Same conventions as in Figure 6.

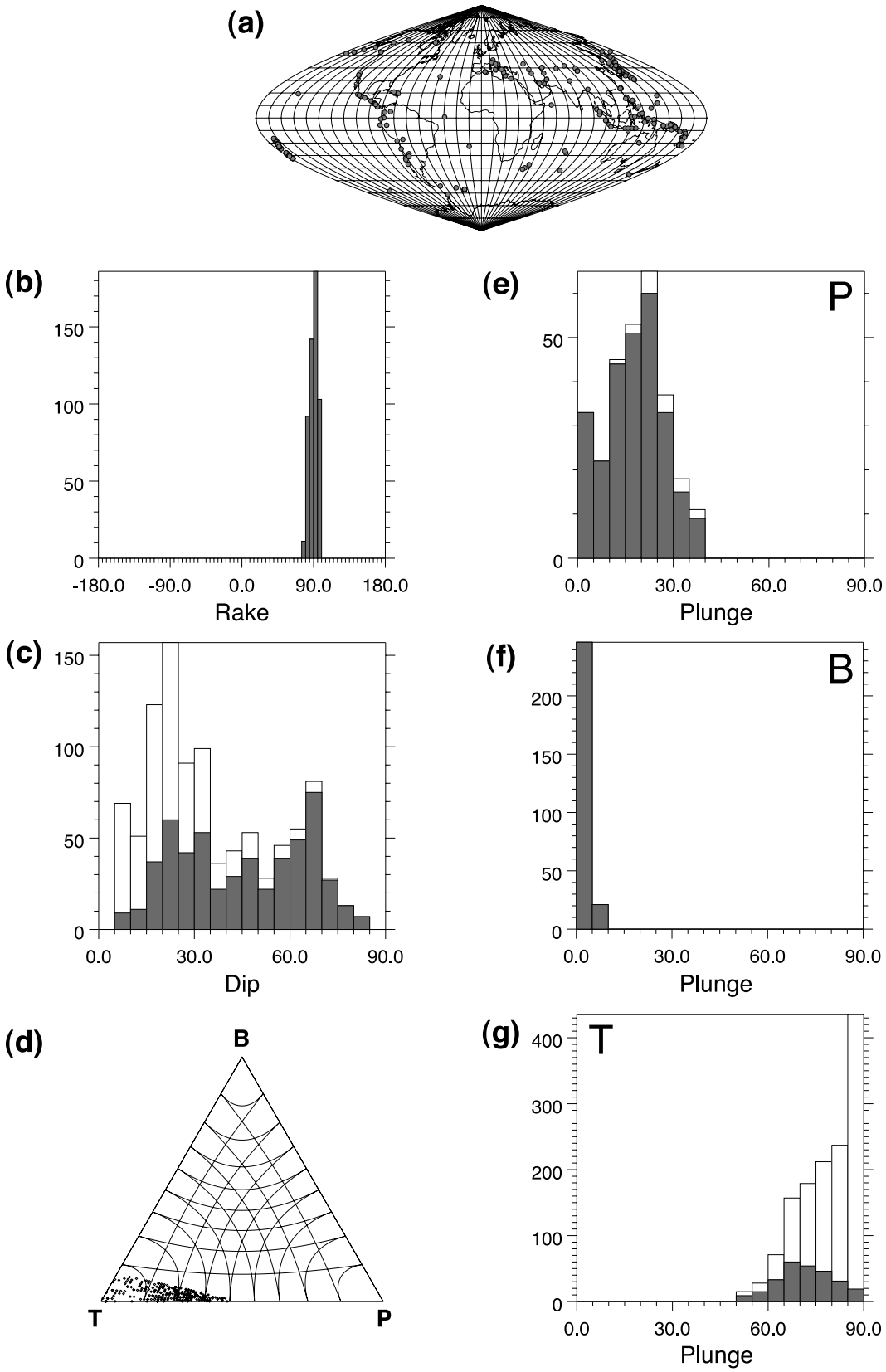

Figure 14. The FD 0–30 R2P data set with depth within the 0–30 km range and with rake within 10° of pure reverse for both nodal planes (267 events, Table 2). Same conventions as in Figure 6.

TABLE 3. Dip and Plunge Modal Values and Inferred Friction Angles[a]

		Fault Plane		Auxiliary Plane		P		*T*	
Data Set	Distribution	Dip	φ_0	Dip	φ_0	Plunge	φ_0	Plunge	φ_0
FD 0–30 R1P	raw	15–25	40–60	65–70	40–50	20–25	40–50	60–65	50–60
FD 0–30 R1P	compensated[b]	15–20	50–60	65–70	40–50	20–30	40–60	85–90	0–10
FD 0–30 R2P	raw	20–25	40–50	65–70	40–50	20–25	40–50	65–70	40–50
FD 0–30 R2P	compensated[b]	20–25	40–50	65–70	40–50	20–25	40–50	85–90	0–10
FD 0–30 N1P	raw	45–50	0–10	30–45	0–30	80–85	10–20	0–5	0–10
		30–45	<0						
FD 0–30 N1P	compensated[b]	45–50	0–10	30–35	20–30	80–90	0–20	0–5	0–10
		30–35	<0	5–10	70–80				
		5–10	<0						
FD 0–30 N2P	raw	45–50	0–10	45 (?)	0 (?)	80–85	10–20	0–5	0–10
FD 0–30 N2P	compensated[b]	45–50	0–10	30–35 (?)	20–30 (?)	80–90	0–20	0–5	0–10
		30–35 (?)	<0 (?)	40–45 (?)	0–10 (?)				

[a]Unit is degrees.
[b]Dip or plunge compensated distribution, as explained in Appendix A.

related by similarities than separated by differences, yet the analysis of these few differences illustrates the contrast between the two selection procedures.

[71] Few rakes from the R1P set deviate by more than 30° from pure reverse (Figure 13b), whereas in the R2P set, the 10° maximum deviation is required (Figure 14b). The relative frequency of steep (>70°) and shallow (<15°) nodal plane dips is lower in the 2P distribution than in the 1P distribution. This is consistent with the analysis in section 6.1: steeply dipping and near-dip-slip planes with shallow dipping and oblique slip second nodal planes are eliminated in the 2P set. This is best illustrated in the triangular representation where data from the R1P set (Figure 13d) along the BA_0 line (defined in Appendix B, Figure B1) are clearly absent from the R2P set (Figure 14d).

[72] The distribution of the nodal plane dip is clearly bimodal (Figures 13c and 14c). The two modes are around 15–25° and 65–70° and are further detailed in Table 3 for the four cases corresponding to R1P or R2P and to raw or density-corrected distributions. These dip modes can be compared with those from former compilations by *Molnar and Chen* [1982], *Triep et al.* [1995], *Frohlich* [2001], and *Sibson and Xie* [1998]. *Molnar and Chen*'s [1982] data are limited to a few convergent zones and are not sorted by rake so that they include mixed strike-slip and reverse mechanisms. They show a 30–60° dip mode. *Triep et al.* [1995] used the CMT database, albeit for the 1977–1992 period and the 0–40 km depth range, and selected reverse events on the basis on *P* and *T* axis plunges. They analyzed the dip distribution of that of the two nodal planes with the lower dip. This yields 15–20° and 40–45° modes. *Frohlich*'s [2001] compilation is also based on the CMT database within the same 0–30 km range as here but for the 1977–1999 period. The events, which are not sorted by rake range, show a cluster corresponding to reverse mechanisms on the triangular representation at 25° from the *T* vertex. This corresponds most closely to the full FD 0–30 km data set triangular diagram cluster (Figure 9d) and *T* axis plunge 65–70° mode (Figure 9g) and remains consistent with the R1P and R2P distribution (Figures 13 and 14). *Sibson and Xie* [1998] compiled 31 earthquakes where the actual fault plane is identified and where slip rake is within 30° of pure reverse. The resulting fault plane dip distribution is bimodal with modes around 25–35° and 45–55° and is limited to dips below 60°. The superposition of the two nodal planes makes a direct comparison difficult, but the low-dip mode remains compatible with, even if not identical to, that of the R2P raw distribution (Figure 14c). Thus, even if the R1P and R2P distributions cannot be directly compared to these various compilations because of their different approaches, they remain roughly consistent with them.

6.3. Strike Slip 0–30 km

[73] Strike-slip events represent between 42% (1P) and 16% (2P) of the 0–30 km data (Table 2) whereas the corresponding 40° rake selection sector represents only 11% of the total rake range. They are located in all types of geodynamic settings (Figures 15a and 16a).

[74] Vertical nodal planes, subvertical *B* axes, and horizontal *P* and *T* axes dominate the orientation distributions (Figures 15 and 16). The similarity between the nodal plane dip distribution (Figures 15c and 16c) and the density-corrected *B* axis plunge distribution (Figures 15f and 16f) could be viewed as reflecting the geometrical constraint that a horizontal slip imposes a *B* axis along the downdip direction of the corresponding nodal plane, hence with a plunge similar to the plane dip. Yet the raw distributions with the same vertical dip modes of the nodal planes but with lower *B* plunges with a 75–85° mode seem to contradict this. This bias toward lower *B* plunges is explained by the fact that a nearly, but not completely, vertical plane with a nearly, but not completely, horizontal slip will yield a *B* axis slightly away from the downdip direction, thus with a plunge lower than the plane dip. This effect is overturned by the density correction that yields a deceptive correspondence.

[75] The difference between the two types of rake selection is best illustrated in this case because this is where the reduction is most stringent, with the S2P set retaining only 39% of the S1P data (Table 2), and the resulting distributions are the most contrasted (Figures 15 and 16). As in the case of reverse events, rake deviations from pure strike slip

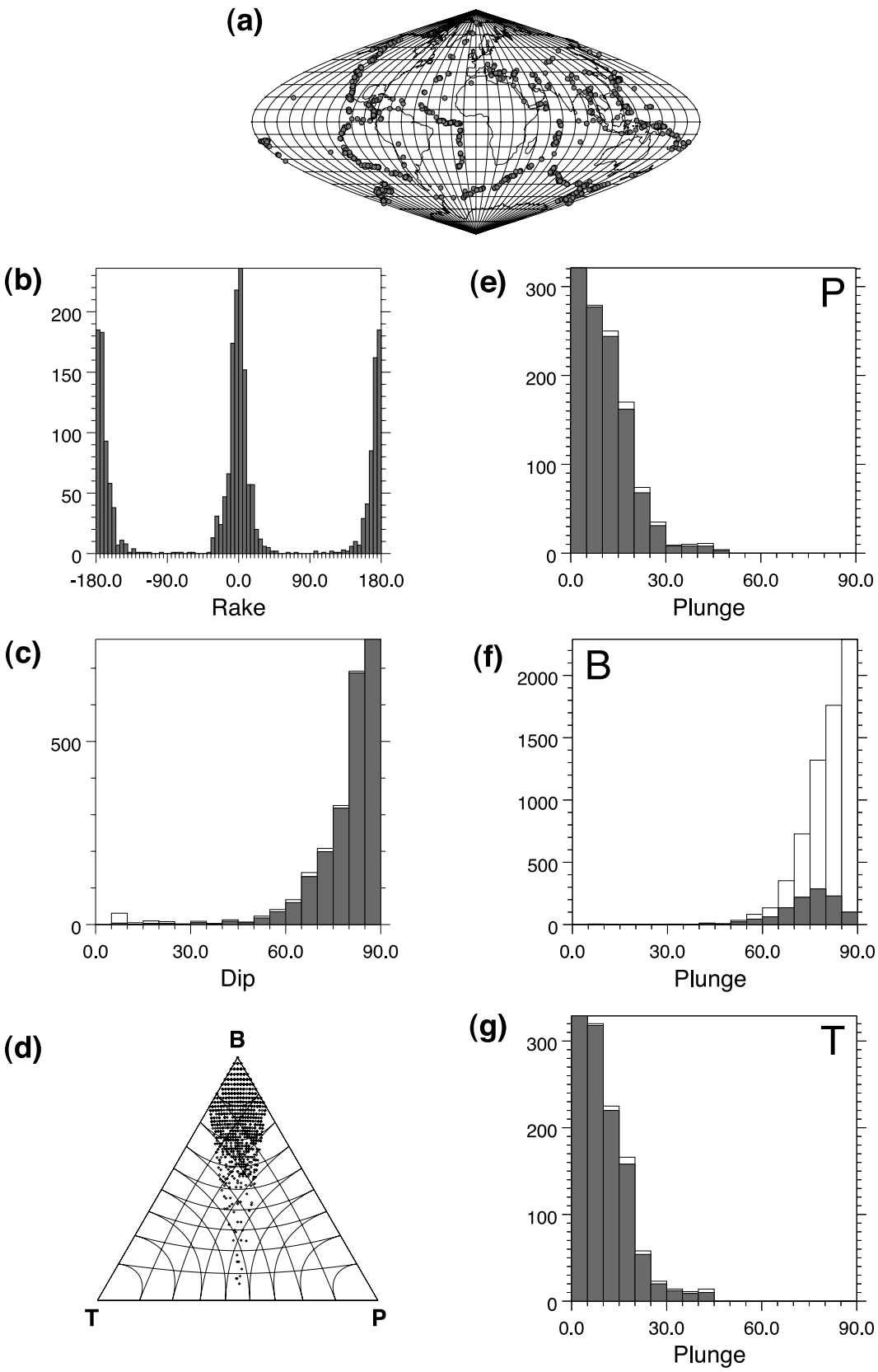

Figure 15. The FD 0–30 S1P data set with depth within the 0–30 km range and with rake within 10° of pure strike for at least one nodal plane (1130 events, Table 2). Same conventions as in Figure 6.

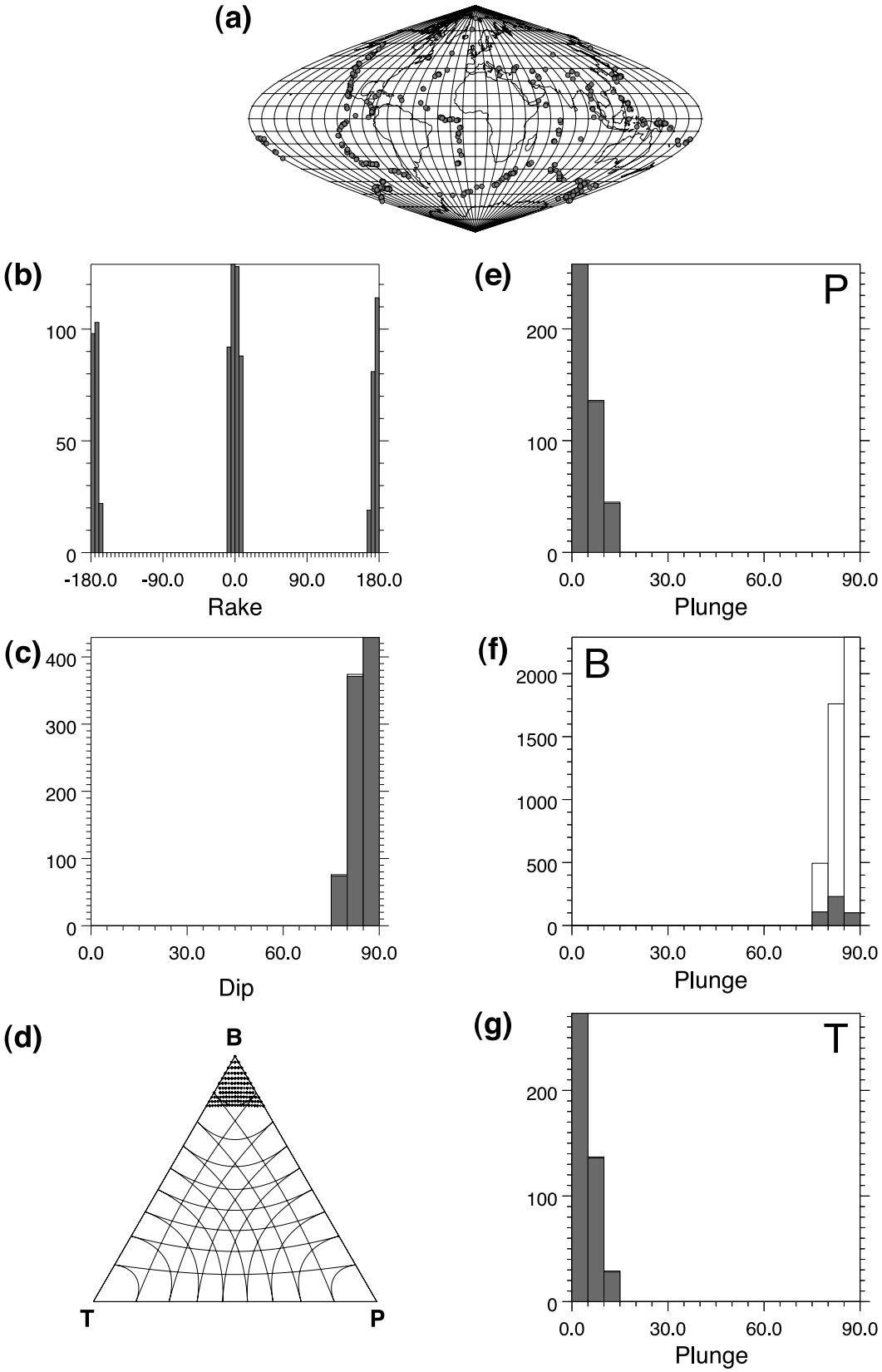

Figure 16. The FD 0–30 S2P data set with depth within the 0–30 km range and with rake within 10° of pure strike for both nodal planes (437 events, Table 2). Same conventions as in Figure 6.

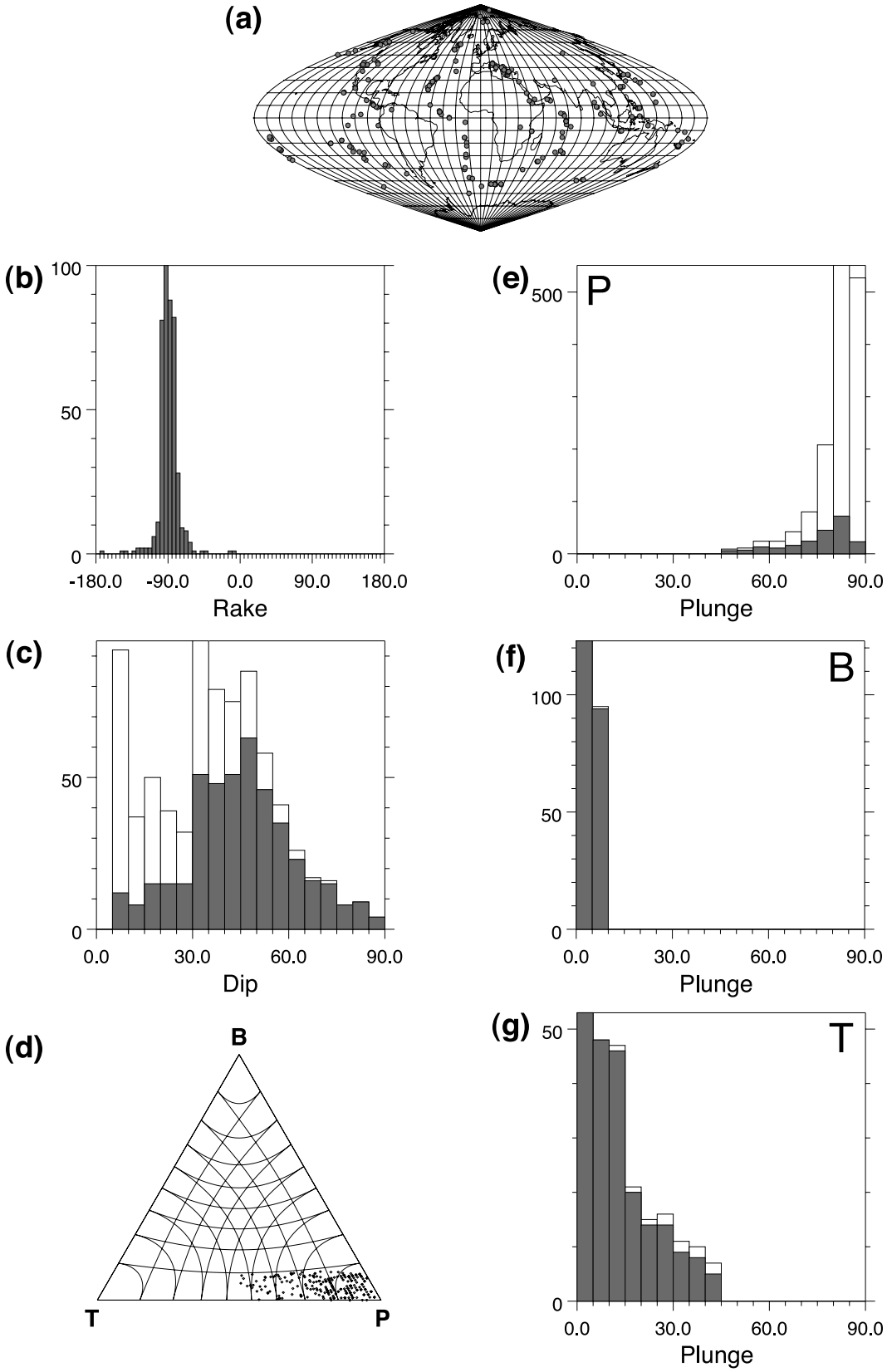

Figure 17. The FD 0–30 N1P data set with depth within the 0–30 km range and with rake within 10° of pure normal for at least one nodal plane (217 events, Table 2). Same conventions as in Figure 6.

are rarely larger than 30° in the S1P set and imposed below 10° in the S2P set. This results in a significantly larger deviation of nodal plane dips from the vertical in the S1P distribution than in the S2P distribution (Figure 15c versus 16c). This is well illustrated in the triangular diagram where the *B* axis may substantially deviate from the vertical and even reach the horizontal in the S1P set (Figure 15d) but remains within 15° of the vertical in the S2P set (Figure 16d). This 10–15° S2P deviation is within the error range of nodal plane dips after the quality selection [*Frohlich and Davis*, 1999].

[76] The S2P subvertical nodal planes and *B* axes are consistent with Andersonian faulting. However, as discussed in section 6.1, the 2P selection has eliminated strike-slip events along shallow dip nodal planes with oblique slip on a second steep nodal plane. Whether a significant number of these S1P events correspond to actual strike slip on low-angle fault depends on which of the two nodal planes is the fault plane. Whereas this can be determined on a regional basis, it remains beyond the scope of this study, and so does the relative importance of actual non-Andersonian strike-slip events in the S1P data.

6.4. Normal 0–30 km

[77] Normal events represent between 8% (1P) and 5% (2P) of the 0–30 km data (Table 2). This is comparable to the corresponding rake selection sector of about 6% of the total range. Two factors limit how much these data are representative of global normal faulting. First, the small size of these samples (217 and 147 for N1P and N2P, respectively) makes them statistically weaker than those for reverse or strike-slip faulting. Second, they are more representative of oceanic than of continental extension because they are dominated by mid-oceanic ridge events (Figures 17a and 18a).

[78] The dip angles of the nodal planes show a single mode at 45° for the raw data and within 30–50° after compensation but with one exception (Figures 17c and 18c and Table 3). The exception is a secondary very low 5–10° dip mode in the N1P compensated distribution (Figure 17c). This secondary mode, however, results from the enhancement by a factor of 8 (Table A1, Appendix A) of a dozen data only, most of which are eliminated in the N2P set, and its significance is therefore uncertain. The constraint that dip-slip nodal planes have complementary dip angles enhances the rise of a 45° mode as dips become close to that value, as illustrated by *Thatcher and Hill* [1991]. This general 45° dip mode can be found in most previous analyses of seismic normal fault dips, whether focusing on the continental domain and related to the debate on low-angle normal faulting [*Jackson*, 1987, 2002; *Jackson and White*, 1989; *Doser and Smith*, 1989; *Thatcher and Hill*, 1991; *Wernicke*, 1995; *Abers et al.*, 1997; *Braunmiller and Nabelek*, 1996; *Hatzfeld et al.*, 2000; *Collettini and Sibson*, 2001] or addressing mid-oceanic ridge earthquakes [*Huang et al.*, 1986; *Jemsek et al.*, 1986; *Huang and Solomon*, 1987, 1988]. These latter studies show typical dip-slip mechanisms with 45° dips of nodal planes and are made all the more relevant by the large proportion of near-oceanic ridge events in the N1P and N2P data sets. The few dip distributions based on the actual fault plane identification consistently show both a 45° dip mode and a cutoff below 30° [*Jackson*, 1987; *Jackson and White*, 1989; *Collettini and Sibson*, 2001].

[79] The *B* axis horizontal mode reflects the dip-slip constraint (Figures 17f and 18f). The horizontal and subvertical modes of the *T* and *P* axes are consistent with the 45° dip mode of nodal planes and the −90° rake mode, except for two notable discrepancies. First, the raw plunge mode of *P* axes is at 80–85° instead of being vertical. Next, the frequency of vertical *P* axes is much less than half the frequency of 45° dip and −90° rake for both nodal planes. This is a reminder that whereas events with both −90° rake and 45° dip correspond to vertical *P* axes, events with either −90° rake or 45° dip, but not both together, correspond to *P* axes deviated from the vertical.

[80] The N2P set retains 68% of the N1P data (Table 2). The N1P rake dispersion (Figure 17b) is similar to that of reverse events (Figure 13b) with few data deviating by more than 30° from dip slip. Similarly to the reverse events situation, the 2P selection eliminates most of the steep (>60°) and shallow (<30°) dip nodal planes from the 1P data set (Figure 18c versus 17c).

7. DISCUSSION

7.1. Extent of Anderson's Faulting

[81] The most striking result for shallow (0–30 km) events is the sharp decline of the frequency of rake from its maxima reached for pure dip slip and strike slip toward its minima reached for oblique slip at 45° from strike or dip and the resulting deficit in oblique slips (Figure 9). A preponderance of Andersonian mechanisms is the simplest way to explain this distribution, even if it is not impossible for peculiar combinations of nonoptimal fault reactivation and nonvertical principal stress systems to account for it.

[82] Pure dip-slip and strike-slip partitioning is still important within the 30–40 km range (Figure 8). Finer shallow depth analysis would require tighter determinations, such as those of *Engdahl et al.* [1998], than those from the U.S. Geological Survey National Earthquake Information Center preliminary determination of epicenter and monthly listing that constitute the overwhelming majority of the CMT catalog hypocenters, with numerous undetermined values set at 10 and 33 km (Figure 4a).

[83] Below 40 km, oblique-slip frequency rises above half that of uniform density, and the modal mechanism is dip slip with subhorizontal *B* axis (Figures 6 and 7). This mode is thus shared between subduction-related events and shallow Andersonian dip-slip events. This explains why the superposition of these two different systems in the global FD data set still yields such well-defined dip-slip and strike-slip modes (Figure 5). The influence of the stress-free surface is thus better expressed by the deficit in 45° oblique slips than by the high frequencies of pure dip slips or strike slips.

[84] The CMT catalog is incomplete for magnitudes $M_w \leq 5.5$ (Figure 19a). This is emphasized by the quality

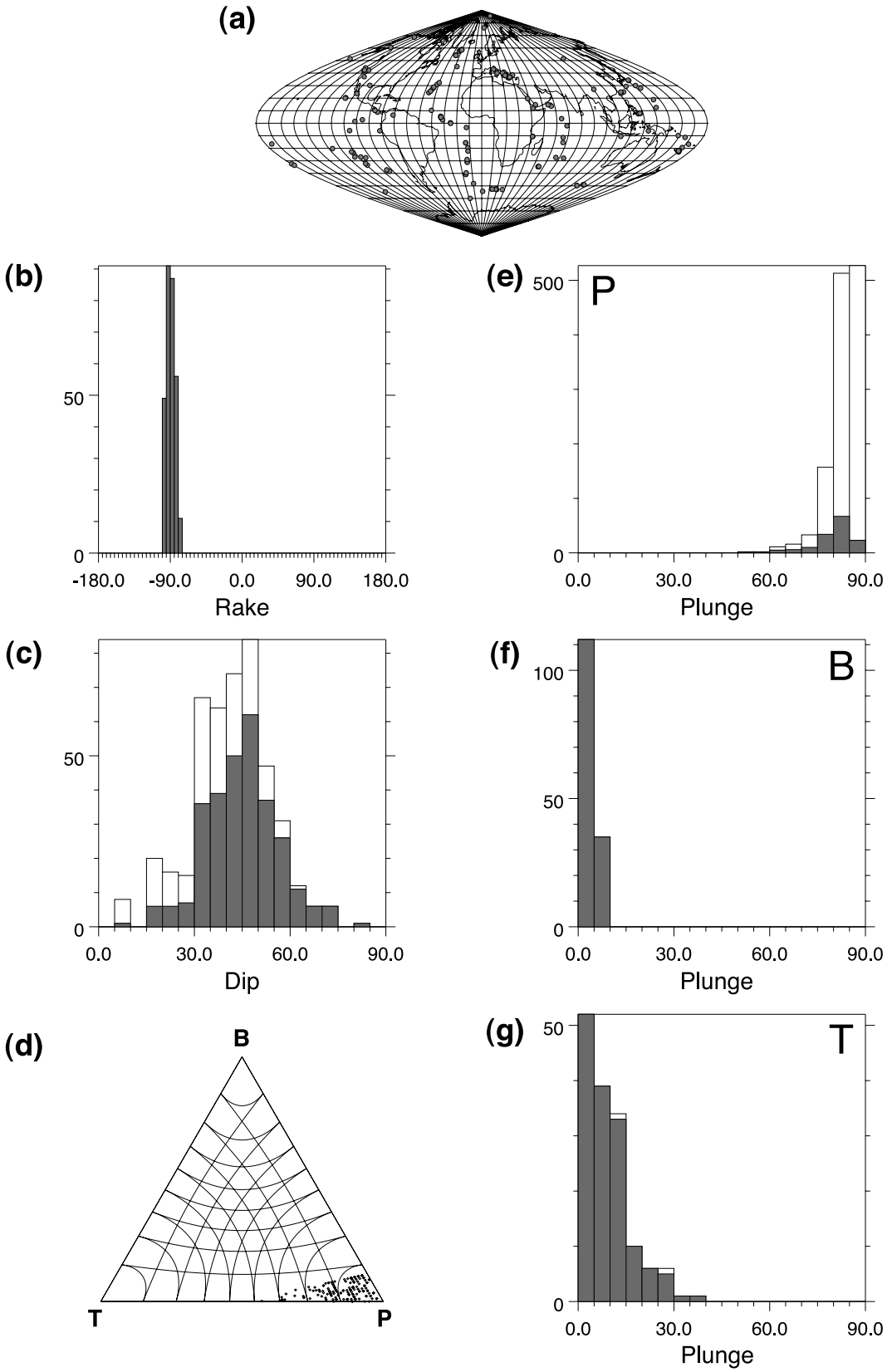

Figure 18. The FD 0–30 N2P data set with depth within the 0–30 km range and with rake within 10° of pure normal for both nodal planes (147 events, Table 2). Same conventions as in Figure 6.

selection that is more severe for small magnitudes (Figure 19b). Yet the sampling remains reasonably representative for $M_w \geq 5.7$ in the FD 0–30 data (Figure 19b) with the most stringent selection (Table 2), as well as in the much smaller pure dip-slip and strike-slip samples (Figures 19c–19e). The preponderance of dip-slip and strike-slip mechanisms is thus established for events above that magnitude only. Another magnitude bias is implicit in the choice of counting the number of events rather than weighting them according to magnitude. This, however, would mainly result in focusing on a few large events and in discarding statistical considerations.

[85] This preponderance of Andersonian regimes is also found in paleostress reconstructions, as shown by a recent compilation [*Lisle et al.*, 2006]. However, this compilation yields extensional, wrench, and compressional regimes frequencies in the ratio 2:2:1, in contrast with the 1:4:2 ratio obtained here. This raises the question of what these two data sets represent. The amount of data, 2208 for paleostress and 2685 for the FD 0–30 data set, is comparable and so are the depths because the paleostress compilation focused on brittle structures. The time span for the seismic data is limited to 28 years whereas that for paleostress is ill defined but most likely measured in Ma. The paleostress sites are all located on continents whereas the seismic data include a significant proportion of oceanic events. However, the most important difference between the two data sets may end up being that whereas the paleostress sites are the result of deliberate individual choices that did not include the goal of yielding a consolidated sample representative of all conditions of deformation, the seismic data set is exhaustive and limited only by a magnitude threshold of $M_w \geq 5.5$. The relative paucity of extensional regimes in the seismic catalog with respect to the paleostress compilation, despite the fact that it includes not only all those from continents but also all those from mid-oceanic ridges, is intriguing. Explanations include a possible sampling bias in the paleostress sites, a longer recurrence time for normal than for other events that would make the 28 years seismic sample unrepresentative, or a bias toward smaller magnitudes for normal faulting. Statistical analyses of earthquake frequency and magnitude [*Okal and Romanovicz*, 1994; *Triep and Sykes*, 1997], including those using seismic catalogs complete down to lower magnitudes than the Global Centroid Moment Tensor catalog [*Frohlich and Davis*, 1993; *Schorlemmer et al.*, 2005], lend support to this last possibility by showing higher b values for normal than for reverse faulting.

7.2. Compensation Versus Consistency

[86] Correcting plunge and dip distribution with respect to uniform spatial density is informative and therefore used here and also often in the literature. Yet it leads to a large emphasis on the highest plunges or lowest dips that may obliterate the data geometrical consistency. For instance, the correspondence between vertical T axes, horizontal B and P axes, and 45° dipping nodal planes (discussed in Appendix B) can be analyzed only in the raw distributions of Figures 9, 10, 13, and 14. The same is true for the correspondence between vertical P axes, horizontal B and T axes, and 45° dipping nodal planes in Figures 9, 10, 17, and 18 and that between vertical B axes, horizontal P and T axes, and vertical nodal planes in Figures 9, 10, 15, and 16. This suggests using both raw and corrected distribution for interpretation.

7.3. Geometry and Mechanical Implications

[87] Isolating Andersonian faulting allows characterizing its geometry and inferring the mechanical properties that control it. In the strike-slip case, selecting rake on both nodal planes instead of on a single one has the most stringent effect with 61% of the S1P events discarded in S2P (Table 2). These events, with inclined B axes, may correspond either to actual strike slip on moderately dipping fault planes or to oblique slip on vertical planes. A significant proportion of odd focal mechanisms with inclined B axes may thus actually correspond to strike slip on moderately dipping planes. Actual strike slip may thus correspond to as little as 39% (S2P) and as much as 100% of the strike-slip mode (S1P). In the first case, it would always correspond to vertical nodal planes and thus would be totally Andersonian. In the second case, nonvertical nodal planes, hence non-Andersonian, events would dominate. Stated otherwise, events with vertical B axes may represent only a fraction, possibly as low as 39%, of actual strike-slip faulting. Analysis of fault mechanical properties requires azimuth constraints that are out of reach for this study but that could be addressed on a regional basis [*Nur et al.*, 1986; *Scotti et al.*, 1991].

[88] In the dip-slip case, selecting rake on both nodal planes instead of on a single one tends to eliminate events with very different nodal plane dips. This selection is thus more stringent in the reverse (51% R2P) than in the normal case (68% N2P) where nodal planes tend to have equivalent dips. Actual dip slip is thus between 68% (N2P) or 51% (R2P) and 100% (N1P or R1P) of the dip-slip mode. In this case, the dip of the fault planes may be related to the apparent friction coefficients by two different approaches.

[89] The first approach relies on the argument made in sections 2.2 and 2.3 that the reactivation of misoriented faults requires a deviation from standard conditions, either in terms of stress difference or in terms of frictional properties, and makes the assumption that the larger such deviations, the less frequent they are. This implies that the frequency of events should decrease as the fault plane orientation gets further away from the optimum. The decreasing frequency of shallow events as rake gets away from the optimal pure dip-slip and strike-slip mechanisms is consistent with this inference (Figure 9b). Relying on this assumption a step further suggests identifying the modal values of the dip of the nodal planes and of the plunge of the P and T axes with the optimal orientations and using them to infer the friction angle (Figure 3).

[90] For reverse events (FD 0–30 R1P and R2P, Figures 13 and 14) this suggests associating the lower and higher nodal plane dip modes with those of the fault and auxiliary plane, respectively. This together with the plunge

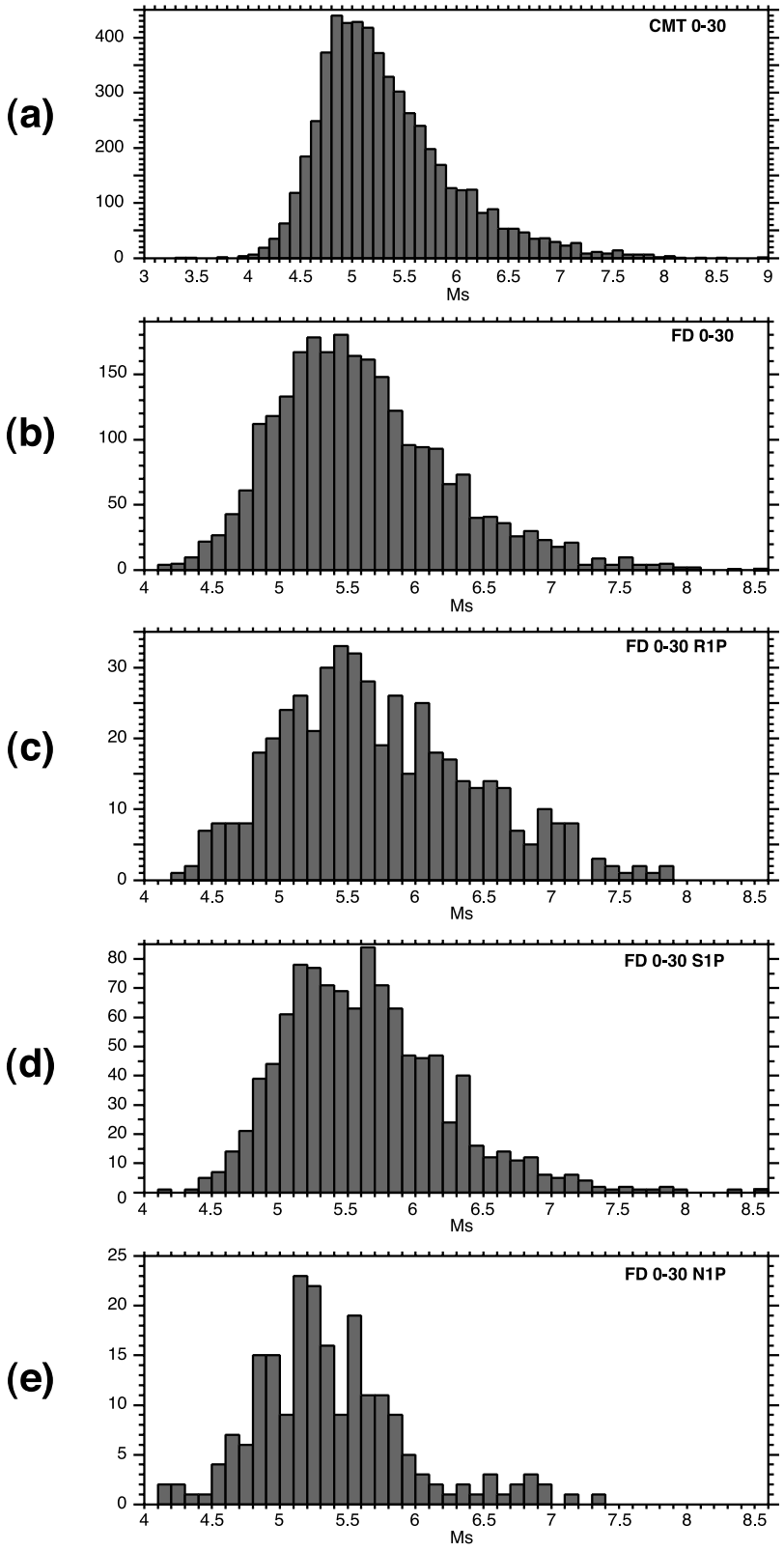

Figure 19. Surface wave magnitude (M_s) histograms for the (a) CMT 0–30, (b) FD 0–30, (c) FD 0–30 R1P, (d) FD 0–30 S1P, and (e) FD 0–30 N1P data sets. In all cases, data without M_s determination are not shown.

modes of the *P* and *T* axes yields a 40–60° friction angle or 0.8 to 1.2 friction coefficient (Table 3). The only discrepancy comes from the *T* axis density-corrected mode that rather suggests a 0–10° friction angle. However, this mode is based on 19 data that are enhanced by a factor of 23 (Table A1, Appendix A) and may therefore indicate that the limits of this correction have been reached. These friction coefficients are higher than the "standard" 31° expected for reactivation but remain within a realistic range between that value and those expected for new faulting.

[91] For normal events (FD 0–30 N1P and N2P, Figures 17 and 18), the plunge modes of the *P* and *T* axes and the 45–50° dip mode of the nodal planes, taken as that of the fault planes, yield 0–20° friction angles (Table 3). Considering the secondary 30–45° dip mode of the nodal planes as that of the auxiliary planes yields 0–30° friction angles; considering it as that of the fault planes would yield a negative friction coefficient. Interpreting the very low 10° N1P compensated dip mode as that of auxiliary planes yields 70–80° friction angles that are unrealistic because they are higher than those for rupture of intact rocks. This confirms that the significance of this mode is uncertain. This approach thus leads to the determination of friction coefficients around 0–20° for normal faults and around 40–60° for reverse faults. This suggests weaker and stronger faults than the expected standard fault with 30° friction coefficient.

[92] The other approach focuses on a much smaller number of events where the fault plane is distinguished from the auxiliary plane and seeks the tail of the dip angle distribution that corresponds to the "lock up" angle, i.e., to the situation where the maximum principal stress direction is within the friction cone and movement is inhibited [*Sibson*, 1994]. This has led to estimates of the lock up dip angle around 30° for normal faults [*Jackson*, 1987; *Jackson and White*, 1989; *Collettini and Sibson*, 2001] and around 60° for reverse faults [*Sibson and Xie*, 1998] that are both consistent with *Byerlee*'s [1978] standard 31° friction angle [*Sibson*, 1994; *Jackson*, 2002].

[93] Thus modal or "lock up" values lead to different friction estimates. This cannot be explained only by the fact that the former are derived from both nodal planes whereas the latter are derived from identified fault planes because, as discussed in sections 6.2 and 6.4, both types of compilations yield comparable dip modal values. Fault rotation, however, affects the signification of the modal values. As deformation accumulates, active fault can rotate from their initial orientation until they reach an attitude beyond the lock up angle that inhibits slip [*Nur et al.*, 1986; *Buck*, 1988, 1993; *Jackson*, 1987; *Jackson and White*, 1989; *Scotti et al.*, 1991; *Thatcher and Hill*, 1991; *Sibson*, 1994; *Sibson and Xie*, 1998; *Hatzfeld et al.*, 2000; *Collettini and Sibson*, 2001]. In the above data sets, such rotations would have to keep a horizontal intermediate principal stress axis within the fault plane because in other cases, maintaining dip-slip mechanisms would become very unlikely, even though not impossible. In these conditions, standard frictional values imply a 60° optimal dip and a 30–90° dip range for active normal faults and a 30° optimal dip and a 0–60° dip range for active reverse faults. Thus, in a given region, the modal dip values may result from the combination of the amount of rotation and of the initial fault orientation, which could be optimal if newly created or nonoptimal if reactivated. How this is compounded in global distributions involving different amounts of finite deformations and various initial orientations is not clear, and the assumption that near-optimal orientation would be statistically favored may not be satisfied.

[94] Yet the asymmetry of the dip modes between normal and reverse events as well as wider dip range in the R2P than N2P distribution still indicate a different behavior between these two type of faulting. Interestingly, these two characteristics can be seen in the distributions provided by studies that identified the actual fault planes [*Jackson*, 1987, 2002; *Jackson and White*, 1989; *Sibson*, 1994; *Sibson and Xie*, 1998; *Collettini and Sibson*, 2001]. This may be related to different fault and stress conditions or to a different rotational organization of the deformation. With a vertical principal stress, the 45° preferred dip cannot help evoking fault zone plasticity [*Byerlee and Savage*, 1992; *Sleep and Blanpied*, 1992; *Rice*, 1992; *Gueydan et al.*, 2004], but stress rotation away from the vertical may provide an alternate explanation [*Yin*, 1989; *Bradshaw and Zoback*, 1988; *Melosh*, 1990; *Wills and Buck*, 1997; *Westaway*, 1999].

8. CONCLUSIONS

[95] Dip-slip and strike-slip mechanisms are the modes of shallow (0–30 km) seismic faulting, and events with oblique slip at 45° from these modes are the least frequent. Events with rakes within 10° of pure dip slip or strike slip represent at least 32% and at most 70% of all well-constrained data shallower than 30 km. This suggests, but does not require, that Andersonian faulting is the mode of shallow seismic faulting and thus appears as a modern vindication of a century old theory. This also supports the idea that the state of stress in the crust is limited by the frictional reactivation of near-optimal preexisting faults, thus extending in scope and depth the validation provided by borehole measurements. Predominating Andersonian conditions explain why *P*, *B*, and *T* axes are often good indicators of stress directions despite sound theoretical objections.

[96] This does not deny the importance of reactivation of nonoptimally oriented planes that is evidenced both by the significant nonmodal values of the rake distributions and by the range of nodal plane dip of pure strike-slip or dip-slip events. In particular, odd events with inclined *B* axes may correspond to the strike-slip reactivation of moderately dipping faults.

[97] Deformation is thus accommodated not only on nearly optimally oriented Andersonian fault planes that produce pure dip slip or pure strike slip but also on nonoptimally oriented planes that result in oblique slip. This can be viewed both as a complication and as an opportunity. The complication is that Anderson's theory obviously does not explain all faulting, as even its author was aware. The opportunity is that if a sufficient number of

events are available, Andersonian and non-Andersonian mechanisms can be separated. The former can then be used to tightly constrain stress orientations, while the latter, together with the just obtained stress orientations, can be used to infer the mechanical properties of the misoriented fault they are associated with.

[98] The asymmetry between normal and reverse faulting suggests different mechanical processes despite similar rocks. This could reflect different properties either of the individual faults or of the fault systems. This questions using the same mechanical considerations to infer the limiting state of stress in extensional and compressional regimes and, in the first case, also questions relying on the same laboratory-derived mechanical properties to explain both types of faults.

[99] This analysis is a testimony of how much global complete and unbiased seismic source parameter catalogs contribute to our understanding of the state of stress and of faulting mechanics. It also underlines how much more could be learned from global catalogs with lower magnitude threshold, better depth constraints, and, above all, more frequent determination of fault versus auxiliary plane.

TABLE A1. Plunge Interval Weighting

Interval Bounds		
Initial	Final	Weight
0	5	1.000
5	10	1.008
10	15	1.023
15	20	1.048
20	25	1.081
25	30	1.126
30	35	1.185
35	40	1.259
40	45	1.355
45	50	1.479
50	55	1.641
55	60	1.859
60	65	2.164
65	70	2.611
70	75	3.322
75	80	4.616
80	85	7.654
85	90	22.904

APPENDIX A: ORIENTATION DENSITY CORRECTION

[100] A uniform density orientation in space yields a cosine frequency distribution on the plunge histograms because of a geometrical bias. Density-corrected histograms are therefore built by correcting the values by a factor that compensates for the variation of the area on a unit sphere covered by each histogram interval.

[101] Taking as reference interval that between plunge p_1 and p_2, the correction, c, to apply to the interval between plunges p_3 and p_4 is given by

$$c = \frac{\sin p_2 - \sin p_1}{\sin p_4 - \sin p_3}. \tag{A1}$$

In this paper the reference is taken as the 0–5° plunge interval, and the resulting correction is given in Table A1. The same correction is applied to the complement of dip, i.e., to the plunge of the normal, for plane orientations.

APPENDIX B: TRIANGULAR DIAGRAMS

[102] The three goals of this appendix are (1) to recall *Frohlich*'s [1992] triangular diagrams definition, (2) to demonstrate that they can be interpreted as a representation of the orientation of the vertical with respect to the *P*, *B*, and *T* axis frame, and (3) to use them to discuss the relationship between the orientations of the *P*, *B*, and *T* axes on one hand and nodal plane dip and slip rake on the other hand.

B1. Frames of Orientation

[103] Let us consider the geographical frame

$$G = (\mathbf{g}_1, \mathbf{g}_2, \mathbf{g}_3), \tag{B1}$$

where $\mathbf{g}_1$, $\mathbf{g}_2$, and $\mathbf{g}_3$ are unit vectors pointing north, east, and down, respectively, and the *P*, *B*, and *T* axis frame defined as

$$A = (\mathbf{a}_1, \mathbf{a}_2, \mathbf{a}_3), \tag{B2}$$

where $\mathbf{a}_1$, $\mathbf{a}_2$, and $\mathbf{a}_3$ are unit vectors chosen along the *P*, *B*, and *T* axes, respectively, so that the frame is direct. Because each vector can be changed into its opposite, there are four frames satisfying these requirements for any given *P*, *B*, and *T* directions. The transformation matrix between *A* and *G* is defined as

$$A^G = \begin{bmatrix} a_{11} & a_{12} & a_{13} \\ a_{21} & a_{22} & a_{23} \\ a_{31} & a_{32} & a_{33} \end{bmatrix}, \tag{B3}$$

where a_{ij} is the *i*th coordinate of $\mathbf{a}_j$ in the frame *G*. Because both *A* and *G* are orthogonal frames of unit vectors, A^G is a unitary matrix, and because both *A* and *G* are direct frames, A^G represents a rotation.

B2. Original Definition

[104] The original definition of the triangular diagrams [*Frohlich and Apperson*, 1992; *Frohlich*, 1992] uses the vector $\mathbf{v}$ made of the third coordinates of each of the *P*, *B*, and *T* axes in the geographical frame:

$$\mathbf{v} = \begin{bmatrix} \sin\delta_P \\ \sin\delta_B \\ \sin\delta_T \end{bmatrix}, \tag{B4}$$

where δ_P, δ_B, and δ_T are the plunge angles of the *P*, *B*, and *T* axes, respectively. Because this vector is unitary it can be represented by its endpoint on the unit sphere. Taking

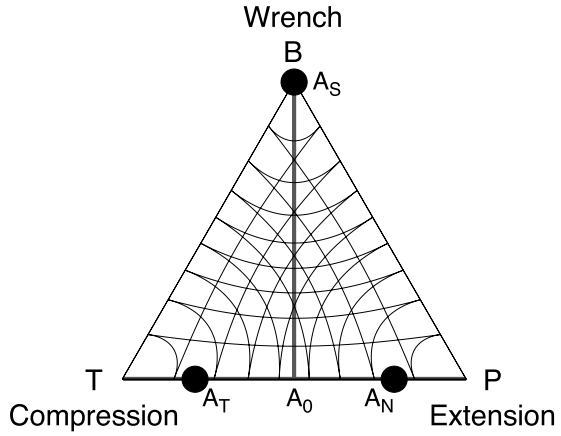

Figure B1. Triangular representation of the orientation of the vertical with respect to the *P*, *B*, and *T* axes. The *P*, *B*, and *T* frame is chosen to be direct. Andersonian faulting in compressional, extensional, and wrench regime plots in A_T, A_N, and A_S, respectively. A_0 is the midpoint between *P* and *T*. Events with one nodal plane with pure strike, pure reverse, and pure normal slip plot in the BA_0, TA_0, and PA_0 segments, respectively. Angular distances every 10° from the vertices are indicated by thin lines.

advantage of the fact that each direction can be exchanged with its opposite allows the restriction of all plunge angles to the [0, 90°] interval and thus the vector to the unit sphere octant with positive coordinates. Projecting this octant into the plane with a gnomonic projection then yields the triangular diagram. The information on the three plunges is thus concentrated in a single diagram by taking into account the fact that they are not independent but constrained to yield orthogonal directions. However, the gnomonic projection does not conserve area so that density computations require either switching to an equal area projection, such as the Lambert azimuthal equal area used in Schmidt stereograms [*Kaverina et al.*, 1996], or using weighting factors [*Frohlich*, 2001].

B3. Relationship With the *P*, *B*, and *T* Frame

[105] The *P*, *B*, and *T* axes and $\mathbf{a}_1$, $\mathbf{a}_2$, and $\mathbf{a}_3$ as defined in section B1 are identical but for a sign indetermination; hence

$$\mathbf{v} = \begin{bmatrix} \sin\delta_P \\ \sin\delta_B \\ \sin\delta_T \end{bmatrix} = \begin{bmatrix} \pm a_{31} \\ \pm a_{32} \\ \pm a_{33} \end{bmatrix}. \tag{B5}$$

It is always possible to choose among the four equivalent direct $\mathbf{a}_1$, $\mathbf{a}_2$, and $\mathbf{a}_3$ frames one for which the three components a_{31}, a_{32}, and a_{33} have the same sign. This allows the reduction of the indetermination to

$$\mathbf{v} = \begin{bmatrix} \sin\delta_P \\ \sin\delta_B \\ \sin\delta_T \end{bmatrix} = \varepsilon \begin{bmatrix} a_{31} \\ a_{32} \\ a_{33} \end{bmatrix}, \tag{B6}$$

where

$$\varepsilon = \pm 1. \tag{B7}$$

Further reduction is not possible because of the conflicting requirements that *P*, *B*, and *T* are constrained to have positive third coordinates whereas $\mathbf{a}_1$, $\mathbf{a}_2$, and $\mathbf{a}_3$ are constrained to be a direct frame.

B4. Alternate Interpretation

[106] The vector $\mathbf{v}$ is thus obtained by the third line of the A^G matrix. However, because A^G is unitary, its transposed matrix is also its inverse matrix:

$$G^A = \left(A^G\right)^{-1} = {}^tA^G, \tag{B8}$$

where

$$G^A = \begin{bmatrix} g_{11} & g_{12} & g_{13} \\ g_{21} & g_{22} & g_{23} \\ g_{31} & g_{32} & g_{33} \end{bmatrix} \tag{B9}$$

and g_{ij} is the *i*th coordinate of $\mathbf{g_j}$ in the *A* frame. Hence

$$\mathbf{g}_3 = \begin{bmatrix} g_{13} \\ g_{23} \\ g_{33} \end{bmatrix} = \begin{bmatrix} a_{31} \\ a_{32} \\ a_{33} \end{bmatrix} \tag{B10}$$

and

$$\mathbf{v} = \varepsilon\, \mathbf{g}_3. \tag{B11}$$

[107] The triangular diagrams can then be interpreted as the representation of the orientation of the upgoing ($\varepsilon = -1$) or downgoing vertical ($\varepsilon = +1$) within the *P*, *B*, and *T* frame. In this paper the vertices are therefore labeled as *P*, *B*, and *T* and chosen along a direct frame (Figure B1).

B5. Relationship Between the *P*, *B*, and *T* Axis Orientations and Nodal Plane Dip and Slip Rake

[108] This triangular representation also provides a relevant framework to consider a few aspects of the geometrical relationship between the orientations of the *P*, *B*, and *T* axes on one hand and nodal plane dip and slip rake on the other hand that are useful for the comprehension of the paper.

[109] Let us first consider the three trivial cases that correspond to the vertices of the triangle (Figure B1). If *P* is vertical, both nodal planes have 45° dip and pure normal dip slip. If *T* is vertical, the dip of the planes is also 45° but with pure reverse dip slip. If *B* is vertical, the nodal planes are vertical with pure strike slip.

[110] If we consider next Andersonian faulting (detailed in Figure 3), strike-slip faulting is expected to plot at the *B* vertex, whereas normal and reverse faulting are expected to plot at positions called A_N and A_T [*Frohlich*, 2001] located $\varphi_0/2 \approx 15°$ away from the *P* and *T* vertices (Figure B1).

[111] Let us now consider the general case of events with one pure dip-slip nodal plane. A necessary and sufficient condition is that B be horizontal. The second nodal plane is thus necessarily also pure dip slip, and the events plot on the TP side of the triangle (Figure B1). Calling A_0 the middle of this side, pure normal events are located on A_0P, and pure reverse events are located on TA_0. The plunges of the P and T axes are obtained by adding $\pm 45^\circ$ to the nodal plane dips.

[112] Let us further consider the general case of events with one pure strike-slip nodal plane. The second nodal plane is thus vertical (its pole is horizontal), and the B axis is along the first nodal plane dip direction. The resulting symmetry implies that P and T have identical plunges. This condition is sufficient to ensure one strike-slip nodal plane. The corresponding events thus plot along the BA_0 line (Figure B1). This leads to two nontrivial conclusions: (1) low B plunge is a better proxy for pure dip slip than high P or T plunge and (2) high B plunge is not a good proxy for pure strike slip.

[113] **ACKNOWLEDGMENTS.** This paper benefited from stimulating exchanges with J. Angelier, M. Bouchon, N. Fry, D. Hatzfeld, and P. Molnar; corrections by J. P. Burg and G. Bokelmann; constructive reviews by C. Frohlich, R. Lisle, and M. Manga; detailed stylistic corrections from R. Lisle; and W. F. Brace's lectures from a long time ago. I dedicate it to the memory of Kei Aki, inspiring professor, who left us on Anderson's faulting centenary.

[114] The Editor responsible for this paper was Michael Manga. He thanks Richard Lisle as the technical reviewer along with one anonymous technical reviewer.

REFERENCES

Abers, G. A., C. Z. Mutter, and J. Fang (1997), Shallow dips of normal faults during rapid extension: Earthquakes in the Woodlark-D'Entrecasteaux rift system, Papua New Guinea, *J. Geophys. Res.*, *102*, 15,301–15,317, doi:10.1029/97JB00787.

Aki, K., and P. G. Richards (1980), *Quantitative Seismology: Theory and Methods*, 932 pp., W. H. Freeman, San Francisco, Calif.

Anderson, E. M. (1905), The dynamics of faulting, *Trans. Edinburgh Geol. Soc.*, *8*, 387–402.

Apperson, K. D., and C. Frohlich (1987), The relationship between Wadati-Benioff zone geometry and P, T and B axes of intermediate and deep focus earthquakes, *J. Geophys. Res.*, *92*, 13,821–13,831, doi:10.1029/JB092iB13p13821.

Arthaud, F. (1969), Méthode de détermination graphique des directions de raccourcissement, d'allongement et intermédiaire d'une population de failles, *Bull. Soc. Geol. Fr., Ser.*, *7*, 729–737.

Bokelmann, G. H. R., and G. C. Beroza (2000), Depth-dependent earthquake focal mechanism orientation: Evidence for a weak zone in the lower crust, *J. Geophys. Res.*, *105*, 21,683–21,695, doi:10.1029/2000JB900205.

Bossu, R., and J. R. Grasso (1996), Stress analysis in the intraplate area of Gazli, Uzbekistan, from different sets of earthquake focal mechanisms, *J. Geophys. Res.*, *101*, 17,645–17,659, doi:10.1029/96JB01182.

Bott, M. H. P. (1959), The mechanics of oblique slip faulting, *Geol. Mag.*, *96*, 109–117.

Brace, W. F. (1964), Brittle fracture of rocks, in *State of Stress in the Earth's Crust*, edited by W. R. Judd, pp. 111–178, Elsevier, New York.

Brace, W. F., and D. L. Kohlstedt (1980), Limits on lithospheric stress imposed by laboratory experiments, *J. Geophys. Res.*, *85*, 6248–6252, doi:10.1029/JB085iB11p06248.

Brace, W. F., B. W. Paulding, and C. Scholz (1966), Dilatancy in the fracture of crystalline rocks, *J. Geophys. Res.*, *71*, 3939–3953.

Bradshaw, G. A., and M. D. Zoback (1988), Listric normal faulting, stress refraction, and the state of stress in the Gulf Coast basin, *Geology*, *16*, 271–274, doi:10.1130/0091-7613(1988)016<0271:LNFSRA>2.3.CO;2.

Braunmiller, J., and J. Nabelek (1996), Geometry of continental normal faults: Seismological constraints, *J. Geophys. Res.*, *101*, 3045–3052, doi:10.1029/95JB02882.

Bucher, W. H. (1920), The mechanical interpretation of joints part I, *J. Geol.*, *28*, 707–730.

Bucher, W. H. (1921), The mechanical interpretation of joints part II, *J. Geol.*, *29*, 1–28.

Buck, W. R. (1988), Flexural rotation of normal faults, *Tectonics*, *7*, 959–973, doi:10.1029/TC007i005p00959.

Buck, W. R. (1993), Effect of lithospheric thickness on the formation of high- and low-angle normal faults, *Geology*, *21*, 933–936, doi:10.1130/0091-7613(1993)021<0933:EOLTOT>2.3.CO;2.

Byerlee, J. D. (1967), Frictional characteristics granite under high confining pressure, *J. Geophys. Res.*, *72*, 3639–3648, doi:10.1029/JZ072i014p03639.

Byerlee, J. D. (1978), Friction of rocks, *Pure Appl. Geophys.*, *116*, 615–626, doi:10.1007/BF00876528.

Byerlee, J. D., and J. C. Savage (1992), Coulomb plasticity within the fault zone, *Geophys. Res. Lett.*, *19*, 2341–2344, doi:10.1029/92GL02370.

Célérier, B. (1988), How much does slip on reactivated fault plane constrain the stress tensor?, *Tectonics*, *7*, 1257–1278, doi:10.1029/TC007i006p01257.

Célérier, B. (1995), Tectonic regime and slip orientation of reactivated faults, *Geophys. J. Int.*, *121*, 143–191, doi:10.1111/j.1365-246X.1995.tb03517.x.

Célérier, B. (2005), Celebrating Anderson's faulting centenary, *Geophys. Res. Abstr.*, *7*, Abstract EGU04-A-06903.

Chen, P. F., C. R. Bina, and E. A. Okal (2004), A global survey of stress orientations in subducting slabs as revealed by intermediate-depth earthquakes, *Geophys. J. Int.*, *159*, 721–733, doi:10.1111/j.1365-246X.2004.02450.x.

Collettini, C., and R. H. Sibson (2001), Normal faults, normal friction?, *Geology*, *29*, 927–930, doi:10.1130/0091-7613(2001)029<0927:NFNF>2.0.CO;2.

Compton, R. R. (1966), Analyses of Pliocene-Pleistocene deformation and stresses in northern Santa Lucia Range, California, *Geol. Soc. Am. Bull.*, *77*, 1361–1380, doi:10.1130/0016-7606(1966)77[1361:AOPDAS]2.0.CO;2.

Coulomb, A. (1776), Sur une application des règles maximis et minimis à quelques problèmes de statique relatifs à l'architecture, *Acad. Sci. Paris Mem. Math. Phys.*, *7*, 343–382.

Doser, D. I., and R. B. Smith (1989), An assessment of source parameters of earthquakes in the cordillera of the western United States, *Bull. Seismol. Soc. Am.*, *79*, 1383–1409.

Dziewonski, A. M., and J. H. Woodhouse (1983), An experiment in systematic study of global seismicity: Centroid-moment tensor solutions for 210 moderate and large earthquakes of 1981, *J. Geophys. Res.*, *88*, 3247–3271, doi:10.1029/JB088iB04p03247.

Dziewonski, A. M., T. A. Chou, and J. H. Woodhouse (1981), Determination of earthquake source parameters from waveform data for studies of global and regional seismicity, *J. Geophys. Res.*, *86*, 2825–2852, doi:10.1029/JB086iB04p02825.

Ekström, G., A. M. Dziewonski, N. N. Maternovskaya, and M. Nettles (2005), Global seismicity of 2003: Centroid-moment tensor solutions for 1087 earthquakes, *Phys. Earth Planet. Inter.*, *148*, 327–351, doi:10.1016/j.pepi.2004.09.006.

Engdahl, E. R., R. Van Der Hilst, and R. Buland (1998), Global teleseismic earthquake relocation with improved travel times and procedures for depth determination, *Bull. Seismol. Soc. Am.*, *88*, 722–743.

Etchecopar, A. (1984), Étude des états de contrainte en tectonique cassante et simulations de déformations plastiques (approche

mathématique), thèse d'État, 269 pp., Univ. des Sci. et Tech. du Languedoc, Montpellier, France.

Frohlich, C. (1992), Triangle diagrams: Ternary graphs to display similarity and diversity of earthquake focal mechanisms, *Phys. Earth Planet. Inter.*, *75*, 193–198, doi:10.1016/0031-9201(92)90130-N.

Frohlich, C. (2001), Display and quantitative assessment of distributions of earthquake focal mechanisms, *Geophys. J. Int.*, *144*, 300–308, doi:10.1046/j.1365-246x.2001.00341.x.

Frohlich, C., and K. D. Apperson (1992), Earthquake focal mechanisms, moment tensors, and the consistency of seismic activity near plate boundaries, *Tectonics*, *11*, 279–296, doi:10.1029/91TC02888.

Frohlich, C., and S. D. Davis (1993), Teleseismic *b* values; Or, much ado about 1.0, *J. Geophys. Res.*, *98*, 631–644, doi:10.1029/92JB01891.

Frohlich, C., and S. D. Davis (1999), How well constrained are well-constrained *T*, *B*, and *P* axes in moment tensor catalogs?, *J. Geophys. Res.*, *104*, 4901–4910, doi:10.1029/1998JB900071.

Gueydan, F., Y. M. Leroy, and L. Jolivet (2004), Mechanics of low angle extensional shear zones at the brittle-ductile transition, *J. Geophys. Res.*, *109*, B12407, doi:10.1029/2003JB002806.

Hafner, W. (1951), Stress distributions and faulting, *Geol Soc. Am. Bull.*, *62*, 373–398, doi:10.1130/0016-7606(1951)62[373:SDAF]2.0.CO;2.

Handin, J. (1969), On the Coulomb-Mohr failure criterion, *J. Geophys. Res.*, *74*, 5343–5348, doi:10.1029/JB074i022p05343.

Hatzfeld, D., V. Karakostas, M. Ziazia, I. Kassaras, E. Papadimitriou, K. Makropoulos, N. Voulgaris, and C. Papaioannou (2000), Microseismicity and faulting geometry in the Gulf of Corinth (Greece), *Geophys. J. Int.*, *141*, 438–456, doi:10.1046/j.1365-246x.2000.00092.x.

Huang, P. Y., and S. C. Solomon (1987), Centroid depths and mechanisms of mid-ocean ridge earthquakes in the Indian ocean, gulf of Aden, and Red Sea, *J. Geophys. Res.*, *92*, 1361–1382, doi:10.1029/JB092iB02p01361.

Huang, P. Y., and S. C. Solomon (1988), Centroid depths of mid-ocean ridge earthquakes: Dependence on spreading rate, *J. Geophys. Res.*, *93*, 13,445–13,477.

Huang, P. Y., S. C. Solomon, E. A. Bergman, and J. L. Nabelek (1986), Focal depths and mechanisms of Mid-Atlantic ridge earthquakes from body waveform inversion, *J. Geophys. Res.*, *91*, 579–598, doi:10.1029/JB091iB01p00579.

Hubbert, M. K. (1951), Mechanical basis for certain familiar geologic structures, *Geol. Soc. Am. Bull.*, *62*, 355–372, doi:10.1130/0016-7606(1951)62[355:MBFCFG]2.0.CO;2.

Isacks, B., and P. Molnar (1969), Mantle earthquake mechanisms and the sinking of the lithosphere, *Nature*, *223*, 1121–1124, doi:10.1038/2231121a0.

Isacks, B., and P. Molnar (1971), Distribution of stresses in the descending lithosphere from a global survey of focal-mechanism solutions of mantle earthquakes, *Rev. Geophys.*, *9*, 103–174, doi:10.1029/RG009i001p00103.

Jackson, J. A. (1987), Active normal faulting and crustal extension, in *Continental Extensional Tectonics*, edited by M. P. Coward, J. F. Dewey, and P. L. Hancock, *Geol. Soc. Spec. Publ.*, 28, 3–17.

Jackson, J. A. (2002), Using earthquakes for continental tectonic geology, in *International Handbook of Earthquake and Engineering Seismology, Part A*, *Int. Geophys. Ser.*, vol. 81A, edited by W. Lee et al., pp. 491–503, Elsevier, New York.

Jackson, J. A., and N. J. White (1989), Normal faulting in the upper continental crust: Observations from regions of active extension, *J. Struct. Geol.*, *11*, 15–36.

Jaeger, J. C. (1959), The frictional properties of joints in rock, *Geofis. Pura Appl.*, *43*, 148–158, doi:10.1007/BF01993552.

Jaeger, J. C. (1960), Shear fracture of anisotropic rocks, *Geol. Mag.*, *97*, 65–72.

Jaeger, J. C. (1962), *Elasticity, Fracture and Flow*, 2nd ed., 268 pp., Methuen, London.

Jaeger, J. C., and N. C. Cook (1979), *Fundamentals of Rock Mechanics*, 3rd ed., 593 pp., Chapman and Hall, London.

Jaeger, J. C., and K. J. Rosengren (1969), Friction and sliding of joints, *Proc. Aust. Inst. Min. Metal.*, *229*, 93–104.

Jemsek, J. P., E. A. Bergman, J. L. Nabelek, and S. C. Solomon (1986), Focal depths and mechanisms of large earthquakes on the Arctic mid-ocean ridge system, *J. Geophys. Res.*, *91*, 13,993–14,005, doi:10.1029/JB091iB14p13993.

Jost, M. L., and R. B. Herrmann (1989), A student's guide to and review of moment tensors, *Seismol. Res. Lett.*, *60*, 37–57.

Kaverina, A. N., A. V. Lander, and A. G. Prozorov (1996), Global creepex distribution and its relation to earthquake-source geometry and tectonic origin, *Geophys. J. Int.*, *125*, 249–265, doi:10.1111/j.1365-246X.1996.tb06549.x.

Kohlstedt, D. L., B. Evans, and S. J. Mackwell (1995), Strength of the lithosphere: Constraints imposed by laboratory experiments, *J. Geophys. Res.*, *100*, 17,587–17,602, doi:10.1029/95JB01460.

Lallemand, S., A. Heuret, and D. Boutelier (2005), On the relationship between slab dip, back-arc stress, upper plate absolute motion, and crustal nature in subduction zones, *Geochem. Geophys. Geosyst.*, *6*, Q09006, doi:10.1029/2005GC000917.

Lisle, R. J., T. O. Orife, L. Arlegui, C. Liesa, and D. C. Srivastava (2006), Favoured states of palaeostress in the Earth's crust: Evidence from fault-slip data, *J. Struct. Geol.*, *28*, 1051–1066, doi:10.1016/j.jsg.2006.03.012.

Lockner, D. A. (1995), Rock failure, in *Rock Physics and Phase Relations: A Handbook of Physical Constants*, edited by T. J. Ahrens, pp. 127–147, AGU, Washington, D. C.

Matsushima, S. (1959), On deformation and fracture of rock (Part IV), deformation and fracture of granite under high confining pressure up to 2000kg/cm^2, *Zisin, Ser. II*, *12*, 68–74.

Matsushima, S. (1960), On the deformation and fracture of granite under high confining pressure, *Bull. Disaster Prev. Res. Inst.*, *36*, 11–20.

McKenzie, D. P. (1969), The relation between fault plane solutions for earthquakes and the directions of the principal stresses, *Bull. Seismol. Soc. Am.*, *59*, 591–601.

McKenzie, D. P., and J. Jackson (1983), The relationship between strain rates, crustal thickening, palaeomagnetism, finite strain and fault movements within a deforming zone, *Earth Planet. Sci. Lett.*, *65*, 182–202, doi:10.1016/0012-821X(83)90198-X.

Melosh, H. J. (1990), Mechanical basis for low-angle normal faulting in the Basin and Range province, *Nature*, *343*, 331–335, doi:10.1038/343331a0.

Mogi, K. (1965), Deformation and fracture of rocks under confining pressure (2), *Bull. Earthquake Res. Inst. Tokyo Univ.*, *43*, 349–379.

Mogi, K. (1966a), Pressure dependence of rock strength and transition from brittle fracture to ductile flow, *Bull. Earthquake Res. Inst. Tokyo Univ.*, *44*, 215–232.

Mogi, K. (1966b), Some precise measurements of fracture strength of rocks under uniform compressive stress, *Rock Mech. Eng. Geol.*, *4*, 41–55.

Mohr, O. (1882), Über die Darstellung des Spannungzustandes eines Korperelementes, *Civilingenieure*, *28*, 113–156.

Molnar, P. (1992), Brace-Goetz strength profiles, the partitioning of strike-slip and thrust faulting at zones of oblique convergence, and the stress-heat flow paradox of the San Andreas fault, in *Fault Mechanics and Transport Properties of Rocks*, edited by B. Evans and T. F. Wong, pp. 435–459, Academic, London.

Molnar, P., and W. P. Chen (1982), Seismicity and mountain building, in *Mountain Building Processes*, edited by K. J. Hsu, pp. 41–57, Academic, London.

Nur, A., H. Ron, and O. Scotti (1986), Fault mechanics and the kinematics of block rotations, *Geology*, *14*, 746–749, doi:10.1130/0091-7613(1986)14<746:FMATKO>2.0.CO;2.

Ohnaka, M. (1973), The quantitative effect of hydrostatic confining pressure on the compressive strength of crystalline rocks, *J. Phys. Earth*, *21*, 125–140.

Okal, E. A., and B. A. Romanovicz (1994), On the variation of *b*-values with earthquake size, *Phys. Earth Planet. Inter.*, *87*, 55–76, doi:10.1016/0031-9201(94)90021-3.

Raleigh, C. B., J. H. Healy, and J. D. Bredehoeft (1972), Faulting and crustal stress at Rangely, Colorado, in *Flow and Fracture of Rocks*, *Geophys. Monogr. Ser.*, vol. 16, edited by H. C Heard et al., pp. 275–284, AGU, Washington, D. C.

Rice, J. R. (1992), Fault stress states, pore pressure distributions, and the weakness of the San Andreas fault, in *Fault Mechanics and Transport Properties of Rocks*, edited by B. Evans and T. F. Wong, pp. 475–503, Academic, London.

Richard, P., and P. Cobbold (1990), Experimental insights into partitioning of fault motions in continental convergent wrench zones, *Ann. Tecton.*, *IV*, 35–44.

Schmidt, W., and H. W. Lindley (1938), Scherung, *Mineral. Petrogr. Mitt*, *50*, 1–28.

Schorlemmer, D., S. Wiemer, and M. Wyss (2005), Variations in earthquake-size distribution across different stress regimes, *Nature*, *437*, 539–542, doi:10.1038/nature04094.

Scotti, O., A. Nur, and R. Estevez (1991), Distributed deformation and block rotations in three dimensions, *J. Geophys. Res.*, *96*, 12,225–12,243, doi:10.1029/91JB00708.

Sheorey, P. R. (1997), *Empirical Rock Failure Criteria*, 176 pp., Balkema, Rotterdam, Netherlands.

Sibson, R. H. (1985), A note on fault reactivation, *J. Struct. Geol.*, *7*, 751–754, doi:10.1016/0191-8141(85)90150-6.

Sibson, R. H. (1994), An assessment of field evidence for 'Byerlee' friction, *Pure Appl. Geophys.*, *142*, 645–662, doi:10.1007/BF00876058.

Sibson, R. H., and G. Xie (1998), Dip range for intracontinental reverse fault ruptures: Truth not stranger than friction?, *Bull. Seismol. Soc. Am.*, *88*, 1014–1022.

Sleep, N. H., and M. L. Blanpied (1992), Creep, compaction and the weak rheology of major faults, *Nature*, *359*, 687–692, doi:10.1038/359687a0.

Snyder, J. P. (1987), Map projections—A working manual, *U.S. Geol. Surv. Prof. Pap.*, *1395*, 383 pp.

Talobre, J. A. (1957), *La mécanique des roches appliquée aux travaux publics*, 444 pp., Dunod, Paris.

Thatcher, W., and D. P. Hill (1991), Fault orientations in extensional and conjugate strike-slip environments and their implications, *Geology*, *19*, 1116–1120, doi:10.1130/0091-7613(1991)019<1116:FOIEAC>2.3.CO;2.

Townend, J., and M. D. Zoback (2000), How faulting keeps the crust strong, *Geology*, *28*, 399–402, doi:10.1130/0091-7613(2000)28<399:HFKTCS>2.0.CO;2.

Triep, E. G., and L. R. Sykes (1997), Frequency of occurrence of moderate to great earthquakes in intracontinental regions: Implications for changes in stress, earthquake prediction, and hazard assessments, *J. Geophys. Res.*, *102*, 9923–9948, doi:10.1029/96JB03900.

Triep, E. G., G. A. Abers, A. L. Lerner-Lam, V. Mishatkin, N. Zakharchenko, and O. Starovoit (1995), Active thrust front of the Greater Caucasus: The April 29, 1991, Racha earthquake sequence and its tectonic implications, *J. Geophys. Res.*, *100*, 4011–4033, doi:10.1029/94JB02597.

Wallace, R. E. (1951), Geometry of shearing stress and relation to faulting, *J. Geol.*, *59*, 118–130.

Wernicke, B. (1995), Low-angle normal faults and seismicity: A review, *J. Geophys. Res.*, *100*, 20,159–20,174, doi:10.1029/95JB01911.

Westaway, R. (1999), The mechanical feasibility of low-angle normal faulting, *Tectonophysics*, *308*, 407–443, doi:10.1016/S0040-1951(99)00148-1.

Williams, A. (1958), Oblique slip faults and rotated stress systems, *Geol. Mag.*, *95*, 207–218.

Wills, S., and W. R. Buck (1997), Stress-field rotation and rooted detachment faults: A Coulomb failure analysis, *J. Geophys. Res.*, *102*, 20,503–20,514, doi:10.1029/97JB01512.

Yin, A. (1989), Origin of regional rooted low-angle normal faults: A mechanical model and its tectonic implications, *Tectonics*, *8*, 469–482, doi:10.1029/TC008i003p00469.

Zoback, M. D., and J. H. Healy (1984), Friction, faulting, and in situ stress, *Ann. Geophys.*, *2*, 689–698.

Zoback, M. D., et al. (1993), Upper-crustal strength inferred from stress measurements to 6 km depth in the KTB borehole, *Nature*, *365*, 633–635, doi:10.1038/365633a0.

B. Célérier, Geosciences Montpellier, Université de Montpellier II, CNRS, Place Bataillon, cc MSE, F-34095 Montpellier CEDEX 5, France. (bernard.celerier@univ-montp2.fr)